Geochemistry, Geophysics, Geosystems®

AGU ADVANCING EARTH AND SPACE SCIENCE

RESEARCH ARTICLE
10.1029/2021GC009845

Sulfur Isotope Constraints on the Petrogenesis of the Kimberley Kimberlites

Angus Fitzpayne[1], Andrea Giuliani[1,2], Nivea Magalhães[3,4], Ashton Soltys[2], Marco L. Fiorentini[5], and James Farquhar[3]

[1]Department of Earth Sciences, Institute for Geochemistry and Petrology, ETH Zürich, Zürich, Switzerland, [2]KiDs (Kimberlites and Diamonds), School of Earth Sciences, The University of Melbourne, Parkville, VIC, Australia, [3]Department of Geology and Earth System Science and Interdisciplinary Centre (ESSIC), University of Maryland, College Park, MD, USA, [4]School of Earth and Environmental Sciences, University of St Andrews, St Andrews, UK, [5]Centre for Exploration Targeting, Australian Research Council Centre of Excellence for Core to Crust Fluid Systems (CCFS), School of Earth Sciences, The University of Western Australia, Crawley, WA, Australia

Key Points:

- S isotopic compositions of fresh, uncontaminated Kimberley kimberlite rocks require a contribution from deeply recycled sedimentary material
- Combining sulfide petrography and S isotope geochemistry elucidates occurrence and origin of deeply subducted volatiles in kimberlite source

Supporting Information:

Supporting Information may be found in the online version of this article.

Correspondence to:

A. Fitzpayne,
angus.fitzpayne@erdw.ethz.ch

Citation:

Fitzpayne, A., Giuliani, A., Magalhães, N., Soltys, A., Fiorentini, M. L., & Farquhar, J. (2021). Sulfur isotope constraints on the petrogenesis of the Kimberley kimberlites. *Geochemistry, Geophysics, Geosystems*, *22*, e2021GC009845. https://doi.org/10.1029/2021GC009845

Received 16 APR 2021
Accepted 24 OCT 2021

Abstract Cretaceous kimberlites in southern Africa have been suggested to host deeply subducted material in their mantle sources based on radiogenic isotope systematics. However, potential subducted material contributions to the volatile budget, including sulfur, of these kimberlites is unclear. Here we report new petrographic, geochemical, and isotopic data on sulfides and sulfates in sub-volcanic kimberlites from Kimberley, South Africa. The examined kimberlites were divided into four groups based on their sulfide mineralogy, sulfur contents, and isotopic compositions. None of these groups exhibit clear signs of mass-independent fractionation. Three samples contain sphalerite, have moderate bulk-sulfide S concentrations (203–329 μg/g) and highly negative bulk-sulfide $\delta^{34}S$ values (−10 to −13‰). Four samples have moderate-to-high bulk-sulfide S contents (220–745 μg/g), positive $\delta^{34}S_{sulfide}$ values (+0.2 to +14‰), and contain galena, pyrite or secondary Cu-sulfides as the dominant sulfides. These groups of S-rich kimberlites were probably contaminated by fluids sourced from local country rocks. The remaining eight samples contain negligible amounts of crustal sulfides (e.g., sphalerite, galena), have lower bulk-sulfide S concentrations (≤111 μg/g), and display a different $\delta^{34}S_{sulfide}$ range (−5.7 to +1.1‰) compared to the S-rich groups. By considering only the five samples with fresh primary Cu-Fe-Ni sulfides, the $\delta^{34}S$ range contracts to between −5.7 and −3.4‰, which is considered representative of the mantle source composition. This range indicates the presence of a deeply recycled sedimentary component in the melt source. The combination of detailed sulfide petrography and S isotope geochemistry in fresh kimberlite rocks provides a further tool to investigate mantle chemical geodynamics through time.

1. Introduction

Kimberlites are small-volume, volatile-rich ultramafic rocks that occur on all of Earth's continents (Giuliani & Pearson, 2019; Jelsma et al., 2009; Tappe et al., 2018), and are formed from magmas that have been emplaced in the upper crust since ~2.8 Ga (Heaman et al., 2019; Tappe et al., 2018). These magmas are thought to be generated by partial melting of Earth's asthenospheric mantle within the diamond stability field (>150 km; e.g., Giuliani et al., 2020; Pearson et al., 2019; Smith, 1983; Stamm & Schmidt, 2017), hence providing insights into the composition of the upper convective mantle beneath continents. This definition does not consider Group II kimberlites or orangeites, which have been recently recognised to be carbonate-rich olivine lamproites (Mitchell, 2020; Pearson et al., 2019) and are sourced in metasomatized portions of the sub-continental lithospheric mantle (Becker & le Roex, 2006; Pearson et al., 2019). Recently, the sources of kimberlite melts have come under increased scrutiny. Woodhead et al. (2019) showed that, at least until around 200 Ma, kimberlites appear to have formed from a relatively homogeneous source with Nd-Hf isotope compositions close to the chondritic uniform reservoir (CHUR) model of Earth's primitive mantle. Giuliani et al. (2021) further argued that this source is equivalent to the PREvalent MAntle (PREMA) component that is widely observed in ocean island and continental basalts. However, kimberlites emplaced since 200 Ma in several large kimberlite provinces (Brazil, western Canada, southern Africa) display initial $^{143}Nd/^{144}Nd$ and $^{176}Hf/^{177}Hf$ ratios that reach significantly lower (i.e., sub-chondritic) values compared to those that have been observed to date in older kimberlites. As discussed by Woodhead et al. (2019), the steep Nd or Hf isotope versus time trend shown by Mesozoic (~180–70 Ma) kimberlites in southern

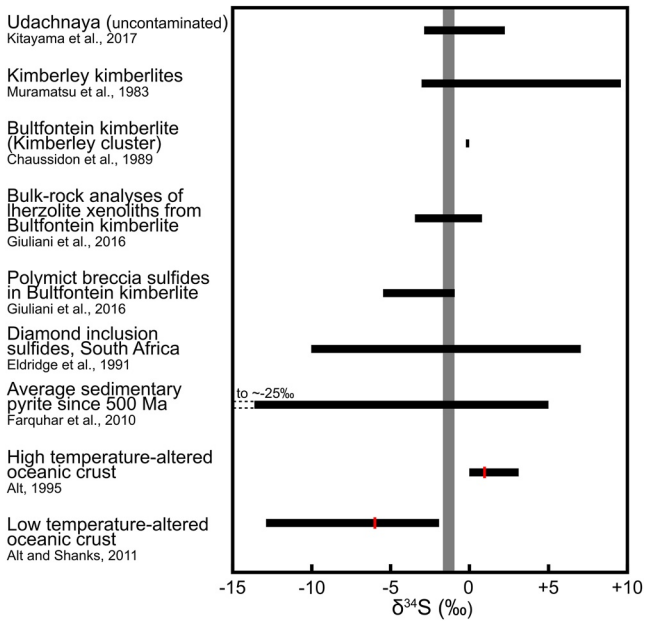

Figure 1. Ranges of sulfur isotopic compositions (black bars) from published studies on the Udachnaya kimberlites (Kitayama et al., 2017), the Kimberley kimberlites (Chaussidon et al., 1989; Muramatsu, 1983), lherzolite and polymict breccia xenoliths from Kimberley (Giuliani et al., 2016), and diamond inclusion sulfides from Jagersfontein (Eldridge et al., 1991). Literature data regarding other terrestrial reservoirs are shown for comparison, including average sedimentary pyrite composition since ~3.8 Ga (Farquhar et al., 2010), as well as oceanic crust altered at high temperature (red line denotes average of +0.9‰; Alt, 1995) and low temperature (red line denotes average of −6.0‰; Alt & Shanks, 2011); gray vertical bar denotes $\delta^{34}S$ range of the asthenospheric mantle source of mid-ocean ridge basalts (−1.3 ± 0.3‰; Labidi et al., 2013).

Africa might relate to either radiogenic ingrowth in a source with unusually high Sm/Nd and Lu/Hf, or to the presence of a recycled crustal component with low $^{143}Nd/^{144}Nd$ and $^{176}Hf/^{177}Hf$ in their mantle source. Combining radiogenic Sr-Nd-Hf data with high-precision $\mu^{182}W$ isotope data is also an effective means of tracing mantle and recycled signatures in kimberlites (Nakanishi et al., 2021; Tappe, Budde, et al., 2020). The studies of Tappe, Budde, et al. (2020), Tappe, Stracke, et al. (2020) also examined kimberlites emplaced >200 Ma, and found similarly decoupled Nd-Hf signatures. The aim of this contribution is to understand the origin of isotopic variability in southern African kimberlites by employing stable isotope geochemistry.

Stable isotope systems are frequently used to investigate the presence of deeply subducted lithospheric components in igneous rocks (e.g., Aubaud et al., 2006; Beunon et al., 2020; Cartigny et al., 2014; Eiler, 2001; Hutchison et al., 2019; Taylor & Sheppard, 1986). However, stable isotope signatures relating to recycled crustal material in the source of worldwide kimberlites have thus far not been definitively identified. For example, most carbonate $\delta^{13}C$ isotope and olivine $\delta^{18}O$ isotope data fall within the expected mantle range, whereas carbonate $\delta^{18}O$ isotopic data are readily affected by post-emplacement hydrothermal alteration (e.g., Castillo-Oliver et al., 2020; Giuliani et al., 2019; Giuliani, Phillips, Kamenetsky, Fiorentini, et al., 2014; Tappe, Budde, et al., 2020; Wilson et al., 2007). Potential exceptions are provided by Li and Cl isotopes, which might record the occurrence of crustal components in kimberlites from West Greenland (Hoare et al., 2021; Tappe, Stracke, et al., 2020). Recently published stable nitrogen isotopic data for mica in mantle xenoliths from the Cretaceous Kimberley kimberlites (South Africa), which were metasomatized by kimberlite melts just before upward transport, might represent the first link between a deeply subducted component and the kimberlite source in southern Africa (Fitzpayne et al., 2019). This is potentially supported by the light $\delta^{34}S$ signature of sulfides in mantle polymict breccia xenoliths from Kimberley (Giuliani et al., 2016), which are considered to represent the products of failed kimberlite eruptions in the lithospheric mantle (Giuliani, Phillips, Kamenetsky, Kendrick, et al., 2014; Lawless et al., 1979; Zhang et al., 2000). However, these isotopic signatures attributed to crustal recycling could also be present in the lithospheric mantle before kimberlite metasomatism and hence might not reflect a melt-source signature. Detailed studies of the stable isotope composition of kimberlites are therefore required to address their source features.

As with carbon, oxygen, and nitrogen, the isotopes of sulfur are also affected by low-temperature processes, and display significant variations between different terrestrial reservoirs (Figure 1). Notably, the sulfur isotopic compositions of mantle-derived continental alkaline magmas including carbonatites were recently interpreted by Hutchison et al. (2019) to demonstrate temporal variations in their melt sources due to changes in the composition of deeply subducted material. In contrast, the S isotopic compositions of kimberlites have rarely been studied. Vinogradov and Ilupin (1972) showed that sulfide and sulfate phases from Yakutian kimberlites ($\delta^{34}S$ = +15 to +52‰, with one value of −14‰) display comparable isotopic compositions to local country rocks ($\delta^{34}S$ = +5 to +44‰). The signature of sulfide and sulfate in the studied Yakutian kimberlites could reflect either a xenocrystic derivation or evidence of significant crustal contamination (Giuliani, Phillips, Kamenetsky, Fiorentini, et al., 2014). The Cl-rich kimberlites at Udachnaya-East (Yakutia) show a much narrower range of $\delta^{34}S_{sulfide}$ (−2.8 to +2.2‰; Kitayama et al., 2017, Figure 1). This range straddles the proposed composition of the asthenospheric mantle (−1.3 ± 0.3‰; Labidi et al., 2013), which Kitayama et al. (2017) employed to propose that crustal contamination did not significantly affect the S isotopic composition of these kimberlites. However, the abundance of late-crystallized sulfates with significantly heavier S isotope compositions (+11.1 ± 1.8‰) in fresh samples from Udachnaya-East (Kitayama et al., 2017) and the very high proportion of sulfates over sulfides in the groundmass of these samples

(D'Eyrames et al., 2017) seem to support a crustal contribution to the late-stage petrogenesis of this kimberlite (i.e., after sulfide crystallisation), as also suggested by other authors (Kopylova et al., 2016).

The sulfur isotope systematics of the Kimberley kimberlites have been investigated previously by Muramatsu (1983), revealing a range of $\delta^{34}S$ values (−3.0 to +9.6‰) in bulk-samples of volcanic breccias and variably altered rocks. Such broad variations might indicate that different processes such as alteration, crustal contamination, and degassing have affected these samples (Giuliani, Phillips, Kamenetsky, Fiorentini, et al., 2014). However, these compositions were not accompanied by sufficient petrographic context to provide a rigorous interpretation. Chaussidon et al. (1989) reported a value of −0.1‰ for pyrrhotite grains from the Bultfontein kimberlite (Kimberley), which is close to the composition of the asthenospheric mantle (−1.3 ± 0.3‰; Labidi et al., 2013). The studies that have been conducted on the Kimberley kimberlites clearly leave some uncertainties as to whether S isotopes can track source features rather than emplacement-related processes in (fresh) kimberlites.

Kimberlites commonly contain small amounts of sulfide and sulfate minerals, which could be of magmatic or secondary origin (D'Eyrames et al., 2017; Giuliani, Phillips, Kamenetsky, Fiorentini, et al., 2014; Mitchell, 1986). Mitchell (1986) noted that nickeliferous sulfides are common kimberlitic accessory minerals, which occur predominantly in the groundmass. This author also suggested that other sulfides can be found in the kimberlite groundmass, albeit reflecting crystallisation at lower temperatures than the nickeliferous phases. A magmatic origin for at least some of these phases is not surprising given the relatively high solubility of sulfur in carbonate-rich and alkaline silicate melts (Chowdhury & Dasgupta, 2020; Helz & Wyllie, 1979; Scaillet & MacDonald, 2006). Mitchell (1995) further described barite as a rare accessory phase in kimberlite rocks, which typically forms in the late stage of kimberlite crystallisation (e.g., De Beers dyke, Kimberley; Soltys et al., 2018a). The Udachnaya-East kimberlite contains a plethora of other sulfate minerals, commonly enriched in alkali metals (e.g., D'Eyrames et al., 2017; Kamenetsky et al., 2004). However, these phases have never been observed in the groundmass of fresh kimberlites elsewhere. Discrimination between a magmatic, hydrothermal, or xenocrystic origin for sulfides and sulfates in kimberlites requires detailed petrographic examination and very few studies have addressed this issue (e.g., D'Eyrames et al., 2017; Sharygin et al., 2007).

To constrain whether deeply subducted crustal material was present in the source of the Kimberley kimberlites, we integrated petrographic observations by means of optical and scanning electron microscopy with bulk-rock major and trace element compositions, and sulfur isotope systematics for hypabyssal (i.e., sub-volcanic) samples from four localities within the Kimberley area (Bultfontein, De Beers, Kimberley Big Hole, and Wesselton; Figure 2). The small size (generally <10–20 μm) of sulfides in most examined samples prevented the application of secondary ion mass-spectrometry (SIMS) analyses to further characterize the S isotopic compositions of these phases. Our new data show that crustal contamination and hydrothermal alteration can variably affect the isotopic composition of sulfur in kimberlites. However, the freshest samples can be employed to pinpoint the isotopic composition of magmatic sulfur and address the role of deep crustal recycling in the source of the Kimberley kimberlites.

2. Samples and Geological Setting

The Kimberley kimberlites were emplaced at ~85–92 Ma (Abersteiner et al., 2019; Batumike et al., 2008; Fitzpayne et al., 2020; Kramers et al., 1983) into a geological succession featuring Permian sedimentary rocks of the Beaufort Group, Carboniferous-to-Permian shales of the Dwyka-Ecca Groups (i.e., Karoo sedimentary rocks), and metamorphosed extrusive igneous rocks and quartzites of the Ventersdorp Supergroup, all intruded by Karoo dolerite dykes and sills (Figure 2; Field et al., 2008; Hanson et al., 2009; Hawthorne, 1975; Shee, 1985). Fragments of these rocks are commonly entrained by the Kimberley kimberlites (e.g., Skinner & Clement, 1979). For example, Wagner (1914) described large mega-blocks ("floating reefs") of Karoo sedimentary rocks within kimberlites from the Kimberley Big Hole and the Wesselton pipes, and similar sedimentary fragments have been found in the De Beers pipe (Wagner, 1914; Williams, 1932). Williams (1932) also noted the presence of sandstone, shale, and dolerite fragments within the Bultfontein kimberlite. The emplacement of the Wesselton sills appears to have been controlled by Karoo dolerite sills, which impeded the progress of kimberlite magma (Hawthorne, 1968), as also suggested for the Benfontein

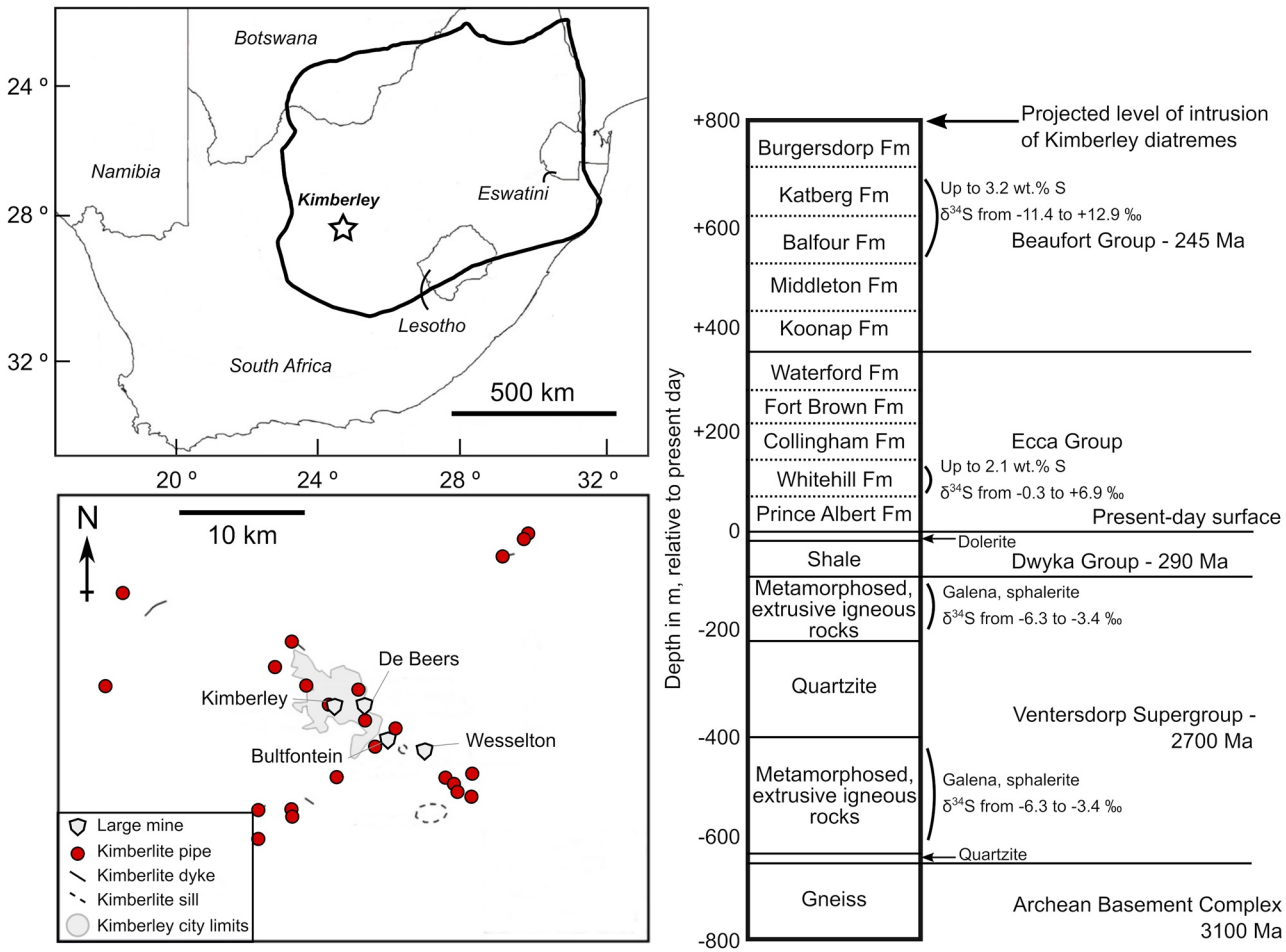

Figure 2. Map of southern Africa, showing outline of Kaapvaal craton (thick black outline) and smaller scale map showing detail of Kimberley area after Field et al. (2008), including large mines from which samples in this study were derived (Bultfontein, De Beers, Kimberley, and Wesselton; gray diamonds), other kimberlite pipes (red circles), kimberlite dykes (solid lines) and sills (dashed lines) and the limits of the town of Kimberley (gray outline). Stratigraphy of Kimberley area also shown based on data from Clement et al. (1986), Smith et al. (1993), and Hanson et al. (2009); S content and isotopic data for studied stratigraphic units taken from Faure and Cole (1999), Maruoka et al. (2003), and Whitelaw et al. (2005).

sill complex in the Kimberley area (Abersteiner et al., 2019; Dawson & Hawthorne, 1973). Further information about the structures of these kimberlites can be found in Field et al. (2008, and references therein).

The 15 kimberlite samples examined in this study were collected from both coherent root-zones (i.e., deep intrusive units) of the Kimberley pipes as well as from dykes and sills (Figure 2). One sample of the Dwyka shale, sourced from outcrop at the Newlands mine (~30–40 km from Kimberley), is also included to examine the effects of crustal contamination. Most of the kimberlite samples were derived from the Wesselton locality, including six samples from the root-zone of this pipe as well as two samples from peripheral dykes, a sample from the Wesselton floor sills complex (WFSC), and two from the Wesselton water tunnel sills (WWTS) Complex. Some of the samples in this study have recently been described in detail by White et al. (2012), Soltys et al. (2018a) Soltys, Giuliani, & Phillips (2020), Soltys, Giuliani, Phillips, & Kamenetsky (2020), and Giuliani et al. (2017, 2019; Table 1). The sample from the Kimberley Big Hole is derived from historical mining of the root-zone of this pipe. In contrast, the kimberlites from the De Beers locality include only samples from the peripheral "Eyebrow" dyke (Clement, 1982; Donaldson & Reid, 1982; Soltys et al., 2018a); the Bultfontein sample is also derived from a dyke (Giuliani et al., 2017).

Table 1
Sample Details and Petrographic Summary of the Kimberley Kimberlites Examined in This Study

Sample	Locality	Petrography	Sulfides	Sulfates	Alteration index
Root-zone					
BHK-1[a]	Kimberley big hole	Moderately altered macrocrystic calcite-serpentine kimberlite	Sphalerite and Fe-Cu sulfides in grondmass and carbonate segregations	Barite in veins cutting through olivine and in carbonate segregations	III
WESK-3 Macro	Wesselton W2	Fresh macrocrystic calcite kimberlite	Ni-Fe-Cu sulfides in groundmass and included in phlogopite rims	Barite in calcite-apatite-serpentine segregations	I
WESK-5	Wesselton W2	Relatively fresh macrocrystic calcite-serpentine kimberlite	Ni-Fe-Cu sulfides with some K and minor native Cu in groundmass and included in calcite	Not observed	II
WESK-6	Wesselton W2	Similar to WESK-5, but more serpentinized	Ni-Fe-Cu, Cu sulfides and native Cu in groundmass serpentine and NiS included in altered olivine	Not observed	III
WESK-7	Wesselton W7	Moderately altered macrocrystic calcite-serpentine kimberlite	dominant NiS and lesser Ni-Fe-Cu and Cu sulfides with native Cu in groundmass and included in altered olivine	Not observed	III
WESK-8	Wesselton W3	Relatively fresh macrocrystic calcite-serpentine kimberlite	Ni-Fe-Cu sulfides and minor native Cu in groundmass and included in calcite	Not observed	II
WESK-9	Wesselton W3	Moderately altered macrocrystic calcite-serpentine kimberlite	Dominant Cu sulfides with native Cu, and lesser Ni and Ni-Fe-Cu sulfides associated with serpentine, included in altered olivine and less commonly in mica	Rare barite, associated with alteration of ilmenite macrocrysts	III
Dykes					
WESK-3 Dyke	Wesselton W2	Fresh aphanitic calcite kimberlite with some flow-banding	Ni-Fe-Cu sulfides in groundmass and included in phlogopite rims	Barite in calcite-apatite-serpentine segregations	I
BK-1	Bultfontein	Fresh moderately macrocrystic calcite-phlogopite kimberlite (details in Giuliani et al., 2017; Soltys et al., 2018b)	Ni-Fe-Cu sulfides in groundmass	Barite in groundmass	I
E310A	De Beers eyebrow dyke	Weakly macrcorystic calcite kimberlite; E310A (altered) displays more signs of alteration than E310F (fresh; details in Soltys et al., 2018a)	Dominant sphalerite and galena with minor pyrite associated with secondary dolomite replacing olivine and monticellite; minor Ni-Fe-Cu sulfides in the groundmass or more rarely as spherical inclusions in olivine	Abundant late-stage barite in groundmass, in carbonate segregations, or included in apatite	IV
E310F	De Beers eyebrow dyke				I
WA-1	Wesselton (contact)	Fresh aphanitic calcite kimberlite	Ni-Fe-Cu sulfides in the groundmass replaced by Cu sulfides, native metals and magnetite; minor galena and pyrite	Barite in secondary veins	I

Table 1
Continued

Sample	Locality	Petrography	Sulfides	Sulfates	Alteration index
Sills					
K-1	Wesselton water tunnel sills	Moderately altered "green" aphanitic kimberlite (details in White et al., 2012)	Dominant pyrite in the groundmass, in carbonate segregations and along mica cleavages; pyrite appears to partly replace less common Fe-Cu sulfides	Barite in groundmass and inclusions in mica rims	III
P-3	Wesselton Water Tunnel Sills	Altered macrocrystic kimberlite sill (details White et al., 2012)	Ubiquitous Fe-Cu-sulfides and galena, and minor djerfisherite and sphalerite in the groundmass	Barite associated with serpentinized olivine	III
WFSC-5	Wesselton Sill Floors	Weakly macrocrystic calcite kimberlite	Galena and Ni-Fe-Cu-sulfides in the groundmass	Barite associated with serpentinized olivine	II

[a]*Note*. that this sample was collected from a sample dump, meaning that its emplacement as a root-zone kimberlite cannot be definitively determined.

3. Methods

Identification and petrographic characterization of sulfides, sulfates and the other kimberlitic minerals was carried out in polished thin section using conventional petrographic microscopes and a Philips (FEI) XL30 environmental scanning electron microscope (SEM) equipped with an OXFORD INCA energy dispersive X-ray spectrometer (EDS) at the University of Melbourne. Back-scattered electron (BSE) images and semi-quantitative chemical analyses were collected using a beam acceleration voltage of 15 kV. Whole-rock major element compositions for most samples were measured at the Geoscience Laboratories of the Ontario Geological Survey in Sudbury, Ontario, Canada. Samples were pulverized in an agate mill to avoid potential contamination from metallic alloys or other incompatible element-enriched media. Major element contents in the samples were analyzed by X-ray fluorescence (XRF) spectrometry. Total loss on ignition (LOI) was determined at 1,000°C under an oxygen atmosphere; the calcined samples were subsequently fused with a borate flux to produce a glass bead for XRF. Carbon contents of samples were measured by infrared absorption after combustion in an oxygen-rich environment. Additional details of the analytical methods are available from the Ontario Geological Survey website (https://www.mndm.gov.on.ca/sites/default/files/2018_geo_labs_brochure.pdf). For whole-rock trace element analyses, small chips of hand samples were selected for their absence of xenolithic material and subsequently powdered using an agate mill at the University of Melbourne. Trace element concentrations were obtained at the University of Melbourne by following the procedures of Eggins et al. (1997) and Kamber et al. (2003). Powdered kimberlite rock samples were first dissolved in 3:1 HF-HNO_3 for 48 hr on a hotplate. Following dilution, a multi-isotope spike was added prior to analysis of the solutions using an Agilent 7700x quadrupole ICP-MS. A solution of USGS dolerite standard W-2 was used as the calibration standard, and two further basalt standards (USGS BCR-2; CRPG BR) were analyzed as unknowns, yielding results consistent with published reference values (Dalton et al., 2019).

Sulfur concentrations and isotope ratios for bulk-sulfide and sulfate fractions were determined at the Stable Isotope Laboratory of the University of Maryland, College Park. Total sulfide, soluble sulfate, and insoluble sulfate were extracted from the same powder (>1 g) through sequential extraction steps. Two different procedures were followed, resulting in two analyses for each component, to ensure the soundness of the data obtained. The strategy for both protocols was to first extract the soluble sulfate pool (e.g., anhydrite) from the rock powder by using ultrapure distilled water (MilliQ: ≥18.2 MΩ.cm). Approximately 20 ml of MilliQ water was added to the sample in a Falcon tube, and then the mixture was flushed with N_2 gas for 5 min. The sample was subsequently centrifuged, and the water was moved into a different Falcon tube. This procedure was repeated twice. The aqueous sulfate was precipitated as $BaSO_4$ with the addition of an acidified solution of 1M $BaCl_2$. After centrifugation and removal of water, the sulfate was analyzed using the Thode solution, which is a mixture of concentrated hydrochloric, hydroiodic, and hypophosphorous acids (52%, 32%, 16%, by volume; Arnold et al., 2014; Thode et al., 1961). In this, and in all steps described below, sulfur was recovered as Ag_2S.

For the first protocol, the remaining powder was then analyzed using a slightly modified version of the procedure described by Labidi et al. (2017). Although there was no expectation of elemental sulfur to be present in these rocks, after extraction of soluble sulfate the remaining powder was soaked in ethanol (reagent grade, anhydrous proof) and flushed with N_2 for 3 hr. There was no identifiable elemental sulfur yield for the samples. Subsequent extraction of sulfur from the rock powder continued with 5N HCl in order to extract acid-volatile sulfur, with a reaction time of 3 hr. The remaining powder was then soaked with ethanol for 3 hr, separated into a boiling flask and run with a chromium-reducible solution (CRS) as described in Canfield et al. (1986), in order to retrieve the remaining sulfide pool. The yields of both acid-volatile sulfide (AVS) and CRS were subsequently combined to represent the total sulfide sulfur pool. The remaining powder was analyzed for insoluble sulfate (e.g., barite) by adding Thode solution for a reaction time of 3 hr.

The second protocol also started with the removal of soluble sulfate as previously described, but the following step consisted of extracting the total sulfide pool from the rock powder with a combined AVS and CRS extraction technique (5N HCl and Cr(II) acidified solution). The solid residue was washed with MilliQ water with the purpose of removing any leftover chromium solution to avoid dilution and hence inefficient extraction of the sulfate fraction as well as potential occurrence of sulfide ions in the sulfate fraction. The residue was analyzed for insoluble sulfate by adding the Thode solution in the same way as the previous extraction.

The silver sulfide extracts from both protocols were kept away from light for one week, after which they were washed with MilliQ water and 1M NH_4OH. Approximately 1–3 mg of Ag_2S was weighed, depending on the sulfur yield of the samples, and wrapped in aluminum foil. These were placed inside a heated nickel vessel, into which fluorine gas was added. The reaction was run overnight to produce SF_6 gas. The SF_6 was purified from potential reaction by-products with cryogenic separation, and further cleaned using gas chromatography. The purified SF_6 gas was collected in a glass manifold, and then the sulfur isotopic composition was measured with a Finnigan MAT 253 dual inlet isotope ratio mass spectrometer by monitoring SF_5^+ ion beams at 127, 128, 129, and 131 Da (daltons).

Sulfur abundances were estimated based on the yield of Ag_2S that was extracted from the original powder. The uncertainties for sulfur abundances were estimated based on a Monte Carlo model of propagation of weighing errors for both the mass of sample powder (±3 mg) and the mass of silver sulfide (±0.15 mg). Some mass loss may occur during extraction of sulfur in the protocols laid out above, however this would be sample specific and difficult to estimate, and this is therefore not accounted for in this estimate. The detection limit for this method of estimation is dependent on the mass balance, and in this case the limit of quantitation is approximately 2x the uncertainty (~0.3 mg). Overall uncertainties for individual sulfide/sulfate fraction S abundances vary between 13 and 16 μg/g (2 s.d.; Table 2). Sulfur isotopic compositions are reported in the standard delta (δ) and capital delta (Δ) notations as units of per mille (‰) using independent measurements of IAEA S-1 and CDT, since a Vienna canyon diablo troilite (VCDT) value for $\Delta^{33}S$ and $\Delta^{36}S$ has not been established. On this scale, IAEA S-1 will have a $\delta^{34}S$ of −0.394‰ and $\Delta^{33}S$ and $\Delta^{36}S$ of 0.116‰ and −0.795‰, respectively. Analytical uncertainties are based on the long-term reproducibility of fluorination analyses of IAEA-S1, which yields 2σ variations of $\delta^{33}S = \pm 0.15‰$, $\delta^{34}S = \pm 0.30‰$, $\delta^{36}S = \pm 0.30‰$, $\Delta^{33}S = \pm 0.016‰$, $\Delta^{36}S = \pm 0.30‰$. Standard reference materials were also analyzed (IAEA-S1, NBS-127) to enable comparisons with previously published data. Furthermore, a parallel study by Geng et al. (2019) provided analysis of two secondary sulfur isotope standards, in which analyses conducted at Maryland returned values within error of the multi-laboratory calibration test, and further validated the soundness of the results obtained.

4. Petrography

The samples from this study are typical hypabyssal kimberlites with macrocrystic or aphanitic texture, and are similar to those previously described from the Kimberley kimberlites (Giuliani et al., 2017; Pasteris, 1980; Shee, 1985; Shee et al., 1994; Soltys et al., 2018a; Soltys, Giuliani, & Phillips, 2020; Soltys, Giuliani, Phillips, & Kamenetsky, 2020; White et al., 2012). Olivine macrocrysts and microcrysts coexist with additional macrocrysts of mantle-derived phases (e.g., phlogopite, garnet, clinopyroxene, ilmenite) in a groundmass of olivine, phlogopite, monticellite, spinel, ilmenite, perovskite, and apatite, which are cemented by

Table 2
Sulfur Content and Isotopic Data for the Kimberley Kimberlites Analyzed in This Study

Sample	Locality	Emplacement	Alteration index	S type	S (ppm)	Total S (ppm)	δ34S	Δ33S	Δ36S	$\Delta 34S_{insoluble\ sulfate\text{-}sulfide}$	$\Delta 34S_{soluble\ sulfate\text{-}sulfide}$
Low-sulfur fresh samples											
WESK-3 Macro	Wesselton W2	Root-zone	I	Insoluble Sulfate		64	−5.05	0.030	0.090		
				Sulfide			−5.06	−0.015	0.161	0.01	
				Sulfide	64		−5.74	−0.007	0.181		
WESK-3 Dyke	Wesselton W2	Dyke	I	Sulfide	43	43	−3.41	−0.012	0.199		
				Sulfide			−5.58	−0.012	0.276		
WESK-5	Wesselton W2	Root-zone	II	Sulfide	111	111	−4.22	−0.008	0.298		
				Sulfide			−3.78	−0.022	0.182		
WESK-8	Wesselton W3	Root-zone	II	Sulfide	64	64	−4.12	−0.017	0.624		
				Sulfide			−5.16	−0.014	0.458		
BK-1	Bultfontein	Dyke	I	Sulfide	83	83	−5.60	−0.055	0.080		
				Sulfide			−5.01	−0.063	0.244		
Low-sulfur partially altered samples											
WESK-6	Wesselton W2	Root-zone	III	Sulfide	80	80	−2.64	−0.010	0.170		
				Sulfide			−1.95	−0.021	0.190		
WESK-7	Wesselton W7	Root-zone	III	Sulfide		61	1.13	−0.025	0.352		
WESK-9	Wesselton W3	Root-zone	III	Insoluble Sulfate	74	128	−2.47	0.007	0.446		
				Sulfide	54		−3.79	0.001	0.227	1.32	
High-sulfur negative-d34S samples											
BHK-1	Big hole	Root-zone	III	Sulfide	203	203	−12.98	0.078	−0.390		
				Sulfide			−12.54	0.060	−0.337		
E310A	De Beers eyebrow dyke	Dyke	IV	Soluble Sulfate	116	560	−10.93	0.010	−0.153		
				Soluble Sulfate			−12.01	−0.039	0.269		
				Insoluble Sulfate	210		−11.71	0.015	0.253		
				Sulfide			−10.75	−0.012	−0.019		−0.80
				Sulfide	235		−10.13	−0.001	0.022	−1.57	−1.26
E310F	De Beers eyebrow dyke	Dyke	I	Insoluble Sulfate	167	495	−9.88	0.004	0.433		
				Sulfide	329		−11.59	0.008	0.129	1.71	
High-sulfur positive-d34S samples											
WA-1	Wesselton (contact)	Dyke	I	Insoluble Sulfate	126	412	−0.73	−0.007	0.038		
				Sulfide	286		0.80	0.006	0.477	−1.53	
				Sulfide			0.75	0.013	0.085		

Table 2
Continued

Sample	Locality	Emplacement	Alteration index	S type	S (ppm)	Total S (ppm)	δ34S	Δ33S	Δ36S	$\Delta 34S_{insoluble\ sulfate\text{-}sulfide}$	$\Delta 34S_{soluble\ sulfate\text{-}sulfide}$
K-1	Wesselton water tunnel sills	Sill	III	Soluble Sulfate	123	1,312	−0.03	0.013	0.004		
				Soluble Sulfate			−0.79	−0.005	0.164		
				Insoluble Sulfate	467		0.06	0.009	−0.029		
				Insoluble Sulfate			0.12	−0.001	0.219		
				Sulfide	723		1.86	−0.003	0.038	−1.80	−1.89
				Sulfide			0.19	−0.004	0.119	−0.07	−0.99
P-3	Wesselton water tunnel sills	Sill	III	Soluble Sulfate	264	1,093	13.00	−0.018	0.266		
				Soluble Sulfate			13.71	−0.053	0.341		
				Insoluble Sulfate	609		11.32	−0.004	0.162		
				Insoluble Sulfate			11.69	−0.032	0.325		
				Sulfide	220		13.87	−0.037	0.185	−2.55	−0.87
				Sulfide			13.71	−0.056	0.310	−2.02	0.00
WFSC-5	Wesselton sill floors	Sill	II	Insoluble Sulfate	129	874	5.66	−0.039	0.359		
				Insoluble Sulfate			7.83	0.006	0.443		
				Sulfide	745		8.42	−0.009	0.105	−2.76	
				Sulfide			7.77	−0.022	0.220	0.06	
Country rock											
Dwyka Shale	Shale	Country rock		Sulfide		12,736	−10.51	0.000	0.078		
				Sulfide			−10.20	0.002	0.841		

interstitial carbonates and serpentine. Sulfide and sulfate phases are typically very scarce and do not occur in contact with each other (Figures 3 and 4). Hydrothermal alteration occurs in the majority of samples and includes widespread groundmass and olivine serpentinization with additional localized mica chloritization, and formation of clays and/or secondary carbonates. Hydrothermal alteration is characterized here using a four-group classification system similar to that which Choi et al. (2020) employed for lamprophyres. In this system, alteration index I means that samples are very fresh and exhibit little (if any) alteration, alteration index IV indicates that the groundmass is largely serpentinized and no fresh olivine is preserved, with alteration indices II and III representing intermediate conditions. The details of this classification for each sample are given in Table 1 together with a summary of sulfide and sulfate petrography, which is also presented below.

Sulfides appear to be predominantly late-crystallized products associated with serpentine, mica and, less commonly, carbonate. Sulfides in thin sections of kimberlites from the root-zones and dykes are very rare and occur mainly as small (5–10 μm) groundmass grains of Ni-Fe-Cu sulfide (predominantly pentlandite and chalcopyrite) or as inclusions in other groundmass phases such as mica (Table 1; Figure 3). The freshest samples (WESK-3 Macro, WESK-3 Dyke, WESK-5, WESK-8 and BK-1; alteration index I and II) show minor signs of sulfide alteration, which is manifested by the partial replacement of sulfide grains with native metals (commonly Cu, Ni), Cu or Ni sulfides, and minor magnetite (Figures 3a–3c). In the samples showing more widespread hydrothermal alteration (e.g., WESK-6, WESK-7 and WESK-9; alteration index III), sulfides are commonly replaced by secondary Cu-sulfide or Ni-sulfide with formation of native metals and magnetite; these phases are ubiquitously associated with serpentine. Samples BHK-1 (root-zone; alteration

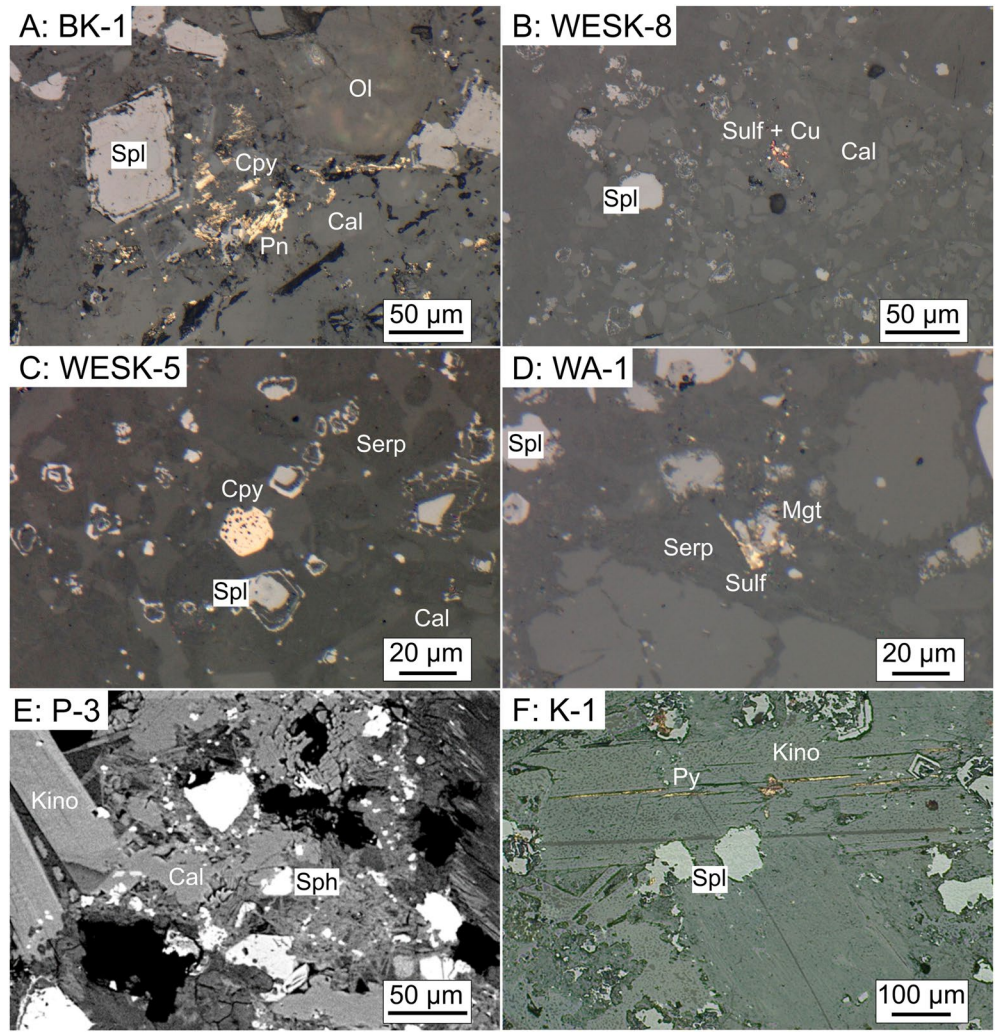

Figure 3. Sulfide petrography. (a) Reflected light photomicrograph of chalcopyrite and pentlandite associated with serpentine, carbonate, and spinel in sample BK-1 ("low-S fresh"); (b) reflected light photomicrograph of tarnished Cu-rich sulfides together with native Cu in the groundmass of sample WESK-8 (low-S fresh); (c) reflected light photomicrograph of a discrete chalcopyrite grain in the groundmass of sample WESK-5 (low-S fresh); (d) reflected light photomicrograph of partially altered Ni-Fe-Cu sulfides in sample WA-1 ("high-S positive $d^{34}S$"), which are associated with serpentine and magnetite; (e) back-scattered electron image of a sphalerite grain in the groundmass of sample P-3 (high-S positive $d^{34}S$); (f) reflected light photomicrograph of pyrite along mica cleavages in sample K-1 (high-S positive $d^{34}S$).

index III), E310F and E310A (Eyebrow dyke; alteration index I and IV, respectively) contain 'exotic' sulfides dispersed in the groundmass including sphalerite, galena and lesser pyrite, which are the dominant sulfides in the Eyebrow dyke. Dyke sample WA-1 (alteration index I) is also unusual because it contains galena and altered sulfides (now native Ni and Cu) associated with magnetite in the groundmass (Figure 3d) as well as pyrite in secondary carbonate-rich inclusions in olivine macrocrysts. Barite is the only sulfate phase observed in the root-zone and dyke samples from the Kimberley kimberlites. Its abundance is variable and it occurs predominantly as a late-crystallizing groundmass phase amongst calcite-serpentine segregations in textural association with apatite, but also included in apatite (Figures 4a and 4b). In samples BHK-1, WA-1 and E310F barite is also found in veins cutting through olivine grains and in carbonate segregations.

Sulfur-bearing phases are more abundant in sills than in the root-zone and dyke samples, being commonly dispersed throughout the groundmass. In the sill samples WFSC-5 and P-3 (Alteration index II and III), sulfides are small (generally ≤10 µm) and predominantly Fe-Cu-Ni-bearing and galena. Sample P-3 also

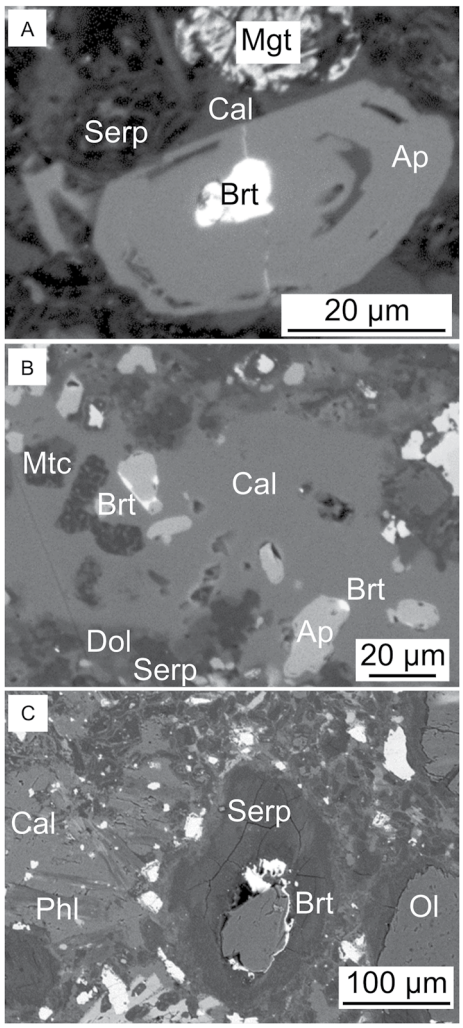

Figure 4. Back scattered electron images of: (a) barite (brt) inclusion and in fractures (white phase) in apatite (Ap) in the groundmass of sample WA-1 (serpentine: Serp; magnetite: Mgt); (b) monticellite (Mtc) and barite (brt) in textural association with apatite (Ap) in calcite (Cal) segregations of sample E310F; (c) barite (Brt) at the contact between olivine (Ol) and pseudomorphic serpentine (Serp) in sample WFSC-5.

contains minor euhedral djerfisherite ($K_6Na(Fe,Cu,Ni)_{25}S_{26}Cl$) in the groundmass, commonly interstitial to kinoshitalite. Minor sphalerite is also present in this sample (Figure 3e). Sill sample K-1 (alteration index III) predominantly contains pyrite (Figure 3f), occurring in the groundmass, along mica cleavages, and in carbonate-rich segregations. There is no apparent correlation between sulfide petrography and alteration conditions in the Kimberley kimberlites (Table 1). In the sill samples, barite remains the only identifiable sulfate phase, occurring in the groundmass, as inclusions in groundmass phases (e.g., apatite, kinoshitalite), or at the contacts between serpentine and olivine (Figure 4c).

5. Geochemistry

5.1. Whole-Rock Major and Trace Element Compositions

The major element compositions of samples examined in this study fall within the range of published compositions of the Kimberley kimberlites (e.g., le Roex et al., 2003, Figure 5; Data Set S1) and other global kimberlite compilations (e.g., Dalton et al., 2019; Tappe et al., 2018, and references therein). Root-zone samples are broadly more SiO_2– (30.6–34.0 wt.%) and MgO-rich (31.0–35.0 wt.%) than dykes and sills (23.6–31.4 wt.% SiO_2; 16.7–29.8 wt.% MgO), but contain less CaO (root-zones: 6.5–11.0 wt.%; dykes and sills: 9.7–17.2 wt.%; Figure 5; Data Set S1). This is consistent with the higher abundance of olivine macrocrysts in the root-zone samples (Figure 6; see also le Roex et al., 2003). Sills also contain slightly more TiO_2 (2.1–5.2 wt.%) and BaO (0.18–0.63 wt.%) than dyke and root-zone samples (1.2–4.0 wt.% TiO_2; 0.05–0.27 wt.% BaO), in line with the aphanitic and highly differentiated nature of kimberlite sills. Trace element ratios in the studied Kimberley kimberlites also overlap with the data from le Roex et al. (2003; Figure S1 in the Supporting Information S1). The samples in this study have experienced negligible crustal contamination, based on various geochemical proxies (e.g., SiO_2 vs. MgO; Gd/Lu vs. SiO_2 – see le Roex et al., 2003), with the exception of samples K-1, P-3 and E310A (Alteration Index III, III and IV, respectively), which show marginally higher SiO_2 contents given their MgO concentrations compared to the other Kimberley kimberlites (Figure 6).

5.2. Whole-Rock S Contents and Isotope Systematics

The eight root-zone and dyke samples that only contain Ni-Fe-Cu sulfides or their alteration products exhibit low abundances of total S (≤128 μg/g; Table 2), consistent with the relatively low abundance of sulfur-bearing phases observed in these samples. Bulk-sulfide (54–101 μg/g) and bulk-sulfate (61–74 μg/g) S concentrations overlap. The remaining seven samples, which also contain sphalerite, galena and/or pyrite, have higher total S contents both in the bulk-sulfide (203–745 μg/g) and bulk-sulfate fractions (up to 873 μg/g; Table 2). There are no clear relationships between bulk-rock S and major elements such as MgO, SiO_2 and CO_2 (Figure S2 in the Supporting Information S1).

Bulk-sulfide fractions in the eight low-S samples have a relatively wide range in $\delta^{34}S$ (−5.7 to +1.1‰; $n = 14$; Figures 7 and 8). However, the five samples with fresh sulfides and Alteration Index I-II ("low-S fresh samples" hereafter) exhibit a more restricted sulfide $\delta^{34}S$ range of between −5.7 and −3.4‰, with the remaining three "low-S partially altered samples" showing sulfide $\delta^{34}S$ values between −3.8 and + 1.1‰ (Table 2). Analyses undertaken with two different extraction methods returned similar values (Figure S3 in the Supporting Information S1; $R^2 = 0.986$, $n = 13$; see Methods). Insoluble sulfate fractions, which correspond to the composition of barite, from three of the low-S samples (both "fresh" and "partially altered"), yield a very

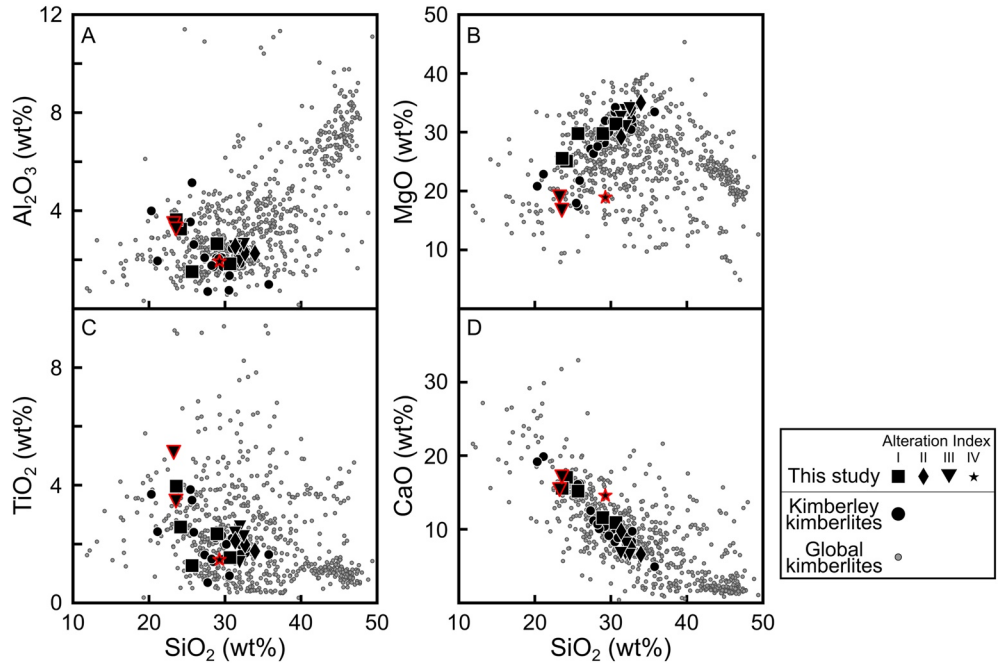

Figure 5. Bulk-rock concentrations of (a) Al_2O_3, (b) MgO, (c) TiO_2, and (d) CaO versus SiO_2 (wt.%) in the Kimberley kimberlites from this study compared to global kimberlites (gray circles; data compilation from Dalton et al., 2019, and references therein) and previous data for the Kimberley kimberlites (black circles; le Roex et al., 2003); sample symbols denote alteration indices after Choi et al. (2020), where squares indicate alteration index I (least altered), diamonds indicate alteration index II, triangles index III and stars index IV (most altered); samples with a red outline display major element evidence of crustal contamination.

similar range in $\delta^{34}S$ to co-existing sulfide fractions (−5.1 to +0.6‰; Figures 9 and S4 in the Supporting Information S1). The $\Delta^{34}S_{sulfate\text{-}sulfide}$ values in these samples are between −0.5 and + 1.3‰ (Figure 10; Table 2).

The remaining seven "high-sulfur samples" can be divided into two groups based on their sulfide petrography and S isotope systematics. Those containing sphalerite as one of the major sulfide phases (E310A, E310F and BHK-1) feature highly negative sulfide $\delta^{34}S$ values of between −10.1 and −13.0‰ (n = 5; hereafter "high-S negative-$\delta^{34}S$ samples"; Figures 7 and 8). Insoluble and soluble sulfates in these kimberlites show similar S isotope compositions to the sulfides ($\Delta^{34}S_{sulfate\text{-}sulfide}$ = −1.6 to +1.7‰; n = 4; Figures 7, 9 and 10 and S4 in the Supporting Information S1; Table 2). The remaining four S-rich samples, which contain abundant galena or pyrite, exhibit highly variable and positive bulk-sulfide $\delta^{34}S$ values of between +0.2

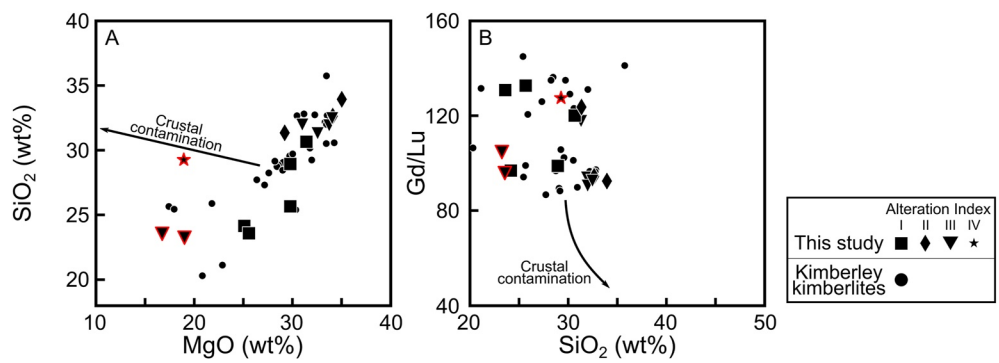

Figure 6. Plots of: (a) SiO_2 (wt.%) versus MgO (wt.%); and (b) Gd/Lu versus SiO_2 (wt.%) in bulk-rock samples of the Kimberley kimberlites in this study, compared to previously published data for the same locality from le Roex et al. (2003, black circles). Process indicators, marked by black arrows, were taken from le Roex et al. (2003). Symbols and symbol colors as in Figure 5.

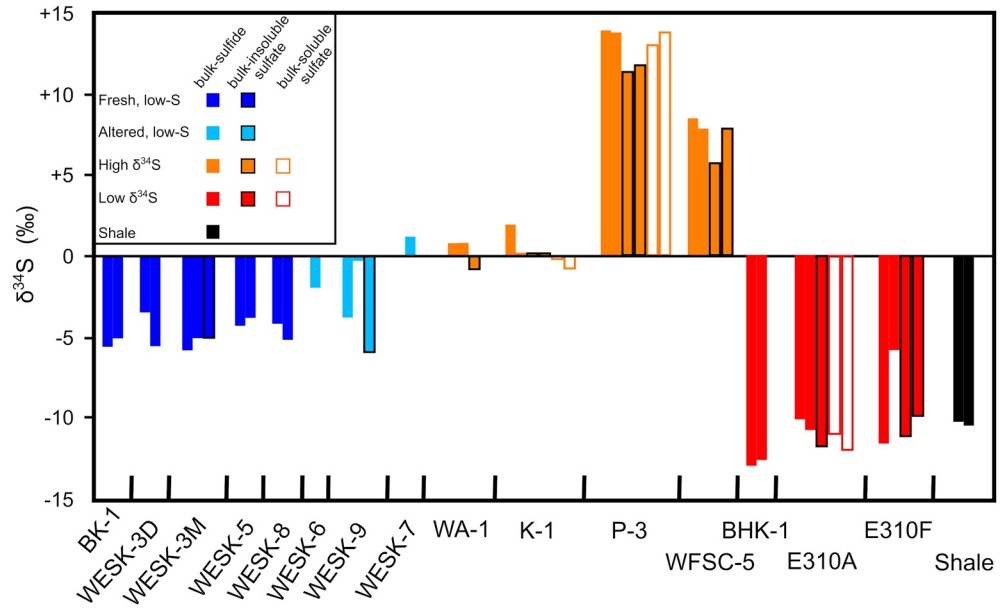

Figure 7. Histogram of whole-rock $\delta^{34}S$ values in the Kimberley kimberlites. Blue bars indicate "low-S fresh" samples, cyan "low-S partially altered" samples, orange "high-S positive-$\delta^{34}S$" samples, red "high-S negative-$\delta^{34}S$" samples, and black bars the Dwyka shale sample analyzed in this study. Bars with no outline represent bulk-sulfide, those with a black outline are bulk-insoluble sulfates, and empty bars with a colored outline are bulk-soluble sulfates; for the shale, only bulk-sulfide analyses are reported.

and +13.9‰ (n = 8; hereafter "high-S positive-$\delta^{34}S$ samples"; Figures 7 and 8). There is limited variability between the sulfur isotope systematics of bulk-sulfate and bulk-sulfide fractions also in these samples ($\Delta^{34}S_{sulfate\text{-}sulfide}$ = −2.8 to +0.1‰; n = 12; Figures 10 and S4 in the Supporting Information S1; Table 2).

A sample of the Dwyka shale country rock was also included in this campaign for comparative purposes. The shale has a high whole-rock S content of 1.2 wt.% and negative sulfide $\delta^{34}S$ values (−10.2 to −10.5‰), which are in the compositional range of the Karoo Permian shale samples analyzed by Maruoka et al. (2003: $\delta^{34}S$ as low as −11.4‰).

There is no simple correlation between sulfide $\delta^{34}S$ and bulk-sulfide S contents (Figure 8) or emplacement conditions (root-zones, dykes, sills; Table 2). Similarly, there is no correlation between sulfate $\delta^{34}S$ or $\Delta^{34}S_{sulfate\text{-}sulfide}$, emplacement conditions and bulk-sulfate or whole-rock S contents (Figures 9 and 10). Sulfur isotopic compositions are not correlated to alteration conditions (Table 2) and major or trace element indicators of crustal contamination (such as bulk-rock ln (Si/Al); Kjarsgaard et al., 2009) or the contamination index of Clement (1982: (SiO2 + Al2O3 + Na2O)/(MgO + 2 × K2O); Figures 10 and S5 in the Supporting Information S1).

Finally, although 27 kimberlite S fractions returned $\Delta^{33}S$ values within uncertainty (≤±0.016‰) of 0, a further 17 analyses, which are found in 10 of the 15 kimberlite samples, display values that are outside of uncertainty of 0 (≥±0.016‰). Small differences in the results returned by the two different analysis methods indicate that only the average $\Delta^{33}S$ values in samples BK-1 (low-S fresh), WESK-7 (low-S partially altered), BHK-1 (high-S negative $\delta^{34}S$), WFSC-5 and P-3 (high-S positive $\delta^{34}S$) are outside of uncertainty of 0 (Table 2; all negative except for BHK-1 and WESK-7). Average kimberlite $\Delta^{36}S$ values are also all within uncertainty of 0 (±0.3‰) except for WESK-8 (low-S fresh), WESK-7, WESK-9 (both low-S partially altered), BHK-1 (high-S negative $\delta^{34}S$), and WFSC-5 (high-S positive $\delta^{34}S$). Values of $\Delta^{33}S$ and $\Delta^{36}S$ in all samples from this study are independent of both the analyzed S fraction (e.g., sulfide $\Delta^{33}S$ from −0.063 to +0.078‰; insoluble sulfate $\Delta^{33}S$ from −0.039 to +0.030‰; soluble sulfate $\Delta^{33}S$ from −0.053 to +0.013‰) and total S contents (Figures 8 and 9). There is no correlation between $\Delta^{33}S$ and $\Delta^{36}S$, making it difficult to infer whether mass-independently fractionated S played a significant role in affecting S isotope signatures in the Kimberley kimberlites.

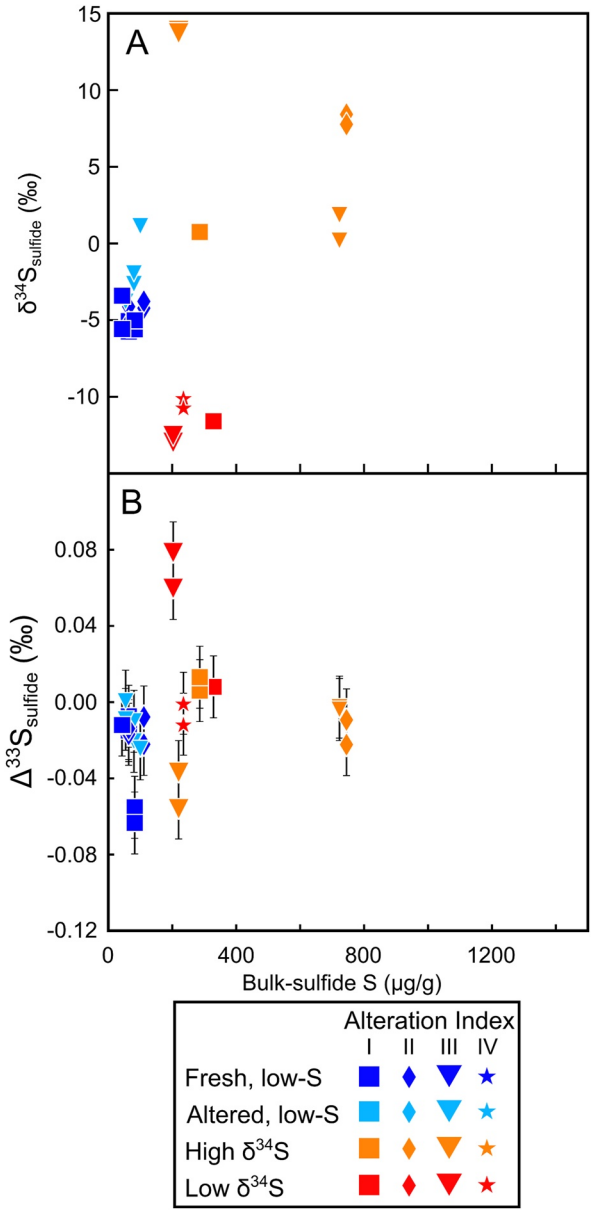

Figure 8. Kimberlite bulk-sulfide (a) $\delta^{34}S$ (‰) and (b) $\Delta^{33}S$ (‰) versus bulk-sulfide S (μg/g) in the Kimberley kimberlites. Symbols as in Figure 5; colors represent different sample groups as described in petrography section, with dark blue for low-S fresh samples, cyan for low-S partially altered samples, orange for high-S positive-$\delta^{34}S$ samples, and red for high-S negative-$\delta^{34}S$ samples. Sulfur abundance and $\delta^{34}S$ error bars (2s) are smaller than symbol size.

6. Discussion

Despite the common magmatic source previously implied for the Kimberley kimberlites based on geochemical and isotopic constraints (e.g., Giuliani et al., 2019, 2021; le Roex et al., 2003; Woodhead et al., 2009, 2019), a wide range in S isotopic compositions has been observed in the sulfide and sulfate fractions (Figures 7–9). In this section, possible mechanisms that might account for the anomalous (i.e., null to negative) $\Delta^{34}S_{sulfate\text{-}sulfide}$ values (Figures 10 and S4 in the Supporting Information S1) are discussed first, before explanations are sought for variable $\delta^{34}S$ values in different kimberlite samples. Finally, we attempt to determine the sulfur isotopic composition of the source of the Kimberley kimberlites and discuss its implications for the occurrence of recycled material in the sub-lithospheric source of Mesozoic southern African kimberlites.

6.1. Sulfate-Sulfide Isotopic Fractionation

The oxidation state of sulfur has a strong influence upon isotopic fractionation between coexisting sulfur-bearing phases (e.g., Bigeleisen & Mayer, 1947; Marini et al., 2011). Sulfate, in which S exists at a higher oxidation state (S^{6+}) than in sulfide (S^{2-}), preferentially incorporates heavier S isotopes. At the temperatures at which kimberlite melts begin to crystallize (~1,000–1,200°C; based on olivine-spinel equilibrium; Fedortchouk & Canil, 2004; Soltys, Giuliani, Phillips, et al., 2020), the experimental work of Miyoshi et al. (1984) and theoretical formulation of Ohmoto and Rye (1979) predict equilibrium $\Delta^{34}S_{sulfate\text{-}sulfide}$ values of between +3.7 to +4.9‰. Kimberlite groundmass crystallisation likely occurs at temperatures below 1,000°C (e.g., Mitchell, 1986), at which point $\Delta^{34}S_{sulfate\text{-}sulfide}$ values are predicted to be >+5‰ (Miyoshi et al., 1984; Ohmoto & Rye, 1979). Alternatively, under hydrothermal conditions in the crust (i.e., T < 400°C; e.g., Stripp et al., 2006), equilibrium $\Delta^{34}S_{sulfate\text{-}sulfide}$ values increase to >+17‰. These ranges contrast strongly with the $\Delta^{34}S_{sulfate\text{-}sulfide}$ observed in this study (−2.8 to +1.3‰; Figure 10; Table 2). These results rule out the possibility that the sulfides and sulfates crystallized from the same melt (or fluid) at equilibrium conditions.

Our petrographic observations show that sulfide and sulfate phases in the kimberlite samples are associated with other late-stage groundmass minerals such as phlogopite, apatite, carbonates and serpentine (Figures 3 and 4). Serpentine in kimberlites is widely considered to be a hydrothermal phase, which probably crystallizes from fluids containing deuteric (i.e., late-stage magmatic) and crustal components (Giuliani, Phillips, Kamenetsky, Fiorentini, et al., 2014, 2017; Mitchell, 2013; Mitchell et al., 2019; Sparks, 2013; Stripp et al., 2006). Barite is also found in late-stage veins cutting through olivine grains and in carbonate segregations (Figure 4). Together, these features demonstrate a late-stage crystallisation of sulfide phases followed by sulfate minerals in these kimberlites (see also Soltys et al., 2018a). Furthermore, some samples contain galena and sphalerite in the groundmass (Figure 3e). These phases do not occur in kimberlite magmas as texturally equilibrated groundmass phases (e.g., Giuliani, Phillips, Kamenetsky, Fiorentini, et al., 2014; Mitchell, 1986), but do occur locally in the crust (e.g., Faure & Cole, 1999; Maruoka et al., 2003; Whitelaw et al., 2005), likely indicating either a xenocrystic origin for these phases or crystallisation from hydrothermal fluids sourced from crustal country rocks. It also seems likely that hydrothermal alteration was responsible for the replacement of primary Ni-Fe-Cu sulfides by secondary assemblages containing variable combinations of native Ni, native Cu, Ni sulfide, Cu sulfide and magnetite observed in most samples (Figures 3b and 3d). Such

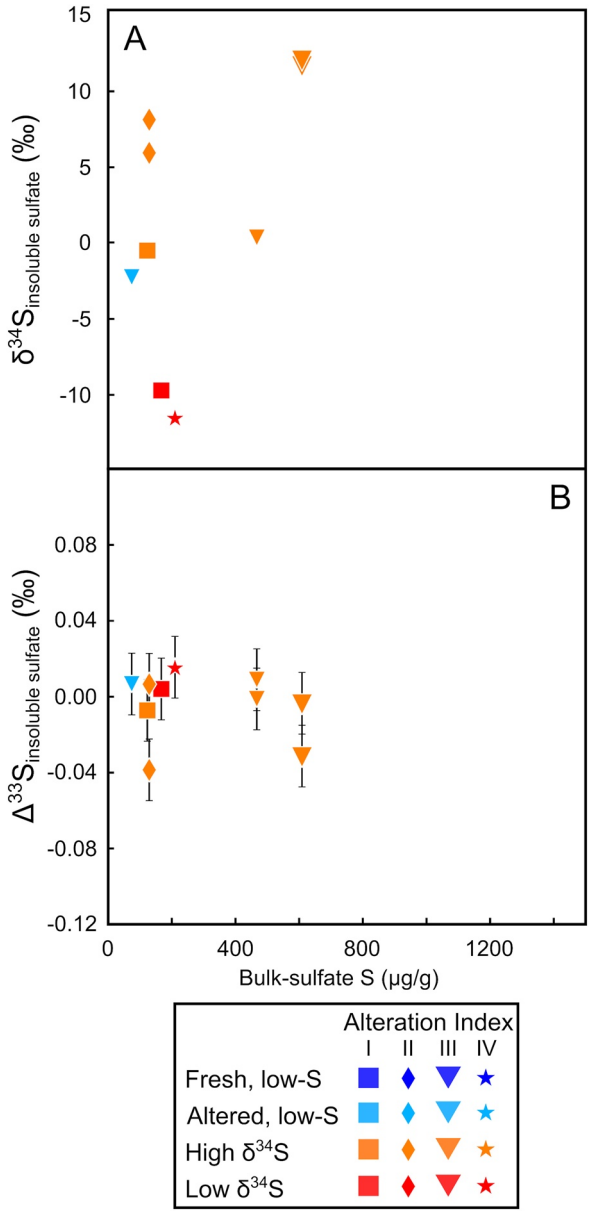

Figure 9. Kimberlite insoluble sulfate (a) $\delta^{34}S$ (‰) and (b) $\Delta^{33}S$ (‰) versus total whole-rock S (µg/g) in the Kimberley kimberlites.

petrographic features indicate that sulfur-bearing phases in many of the kimberlite samples from this study are not strictly magmatic, but also include crustal components. Notably, apatite in many of these samples contains very little SO_3 (<0.05 wt.%; Soltys, Giuliani, & Phillips, 2020), suggesting that it does not contribute in a significant way to bulk-sulfate S isotopic systematics.

At the relatively low temperature of sulfate crystallisation in kimberlites (<600°C; Kitayama et al., 2017), sulfates can have a similar isotopic composition to sulfides from the same sample (i.e., no isotopic fractionation) if the isotopic composition of the residual melt/fluid changes before sulfate crystallisation (i.e., after sulfide formation), for example due to crustal assimilation (e.g., Rye, 2005). However, in the Kimberley kimberlites, $\Delta^{34}S_{sulfate\text{-}sulfide}$ is relatively constant (Figure S4 in the Supporting Information S1) and independent of crustal contamination, bulk-sample S contents and $\delta^{34}S$ values (~−11 to ~+13‰; Figure 10; Table 2). This observation requires a different process to form sulfates with similar S isotope compositions to co-existing sulfides. Sulfates that are derived from the oxidation of sulfide minerals (or H_2S in fluids) can exhibit similar $\delta^{34}S$ values to pre-existing sulfides if equilibrium between SO_4^{2-}-bearing fluids and residual sulfides elsewhere in the same rock volume is not attained (Rye, 2005). Sulfur isotopes can also be kinetically fractionated during low-temperature oxidation of sulfides, with preferential retention of the heavier S isotopes in the residual sulfides and partitioning of the lighter S isotopes into the oxidized fluid (Delacour et al., 2008; Fry et al., 1988), that is, the opposite of equilibrium fractionation.

In the Kimberley kimberlites, sulfates and sulfides are very scarce and never in contact with each other, which implies that isotopic equilibration through in-situ (partial) replacement of sulfides by sulfates did not occur. The common association of barite with serpentine instead suggests sulfate crystallisation from SO_4^{2-}-bearing hydrous fluids. During hydrothermal alteration, wholesale conversion of sulfide to sulfate will likely result in the creation of an acidic environment and soluble species, via a reaction such as:

$$FeS_2 + 3.5\,O_2 + H_2O = Fe^{2+} + 2SO_4^{2-} + 2H^+$$

The reaction above suggests that sulfate ions are mobilized in hydrous fluids, likely leading to sulfate reprecipitation commonly associated with hydrous minerals such as serpentine, which is indeed observed in the Kimberley kimberlites (Figure 4c). This hypothesis is valid only if the sulfate-forming fluids did not equilibrate with residual sulfides in the same kimberlite before sulfate precipitation. If some equilibration occurred, $\Delta^{34}S_{sulfate\text{-}sulfide}$ would be strongly positive (e.g., >5‰ - see above), which is the opposite of what is observed in the Kimberley samples (−2.8 to +1.7‰; Table 2; Figure 10 and S4 in the Supporting Information S1).

Barite in hydrothermal environments crystallizes from hydrous fluids with decreasing temperature or, more commonly, after interaction between hydrothermal fluids and meteoric waters (Hanor, 2000). Fluid mixing leads to fast precipitation of barite under conditions of isotopic disequilibrium (Rye, 2005) and, perhaps in combination with kinetic fractionation, could explain the anomalous isotopic composition of bulk-insoluble sulfates (i.e., barite) in the Kimberley kimberlites. This contrasts with the case of the Udachnaya-East kimberlite where sulfates represent a significant magmatic component of the groundmass (D'Eyrames et al., 2017) and indeed sulfate-sulfide S isotope fractionation is recorded for geologically reasonable conditions (~500–600°C; Giuliani, Phillips, Kamenetsky, Fiorentini, et al., 2014; Kitayama et al., 2017).

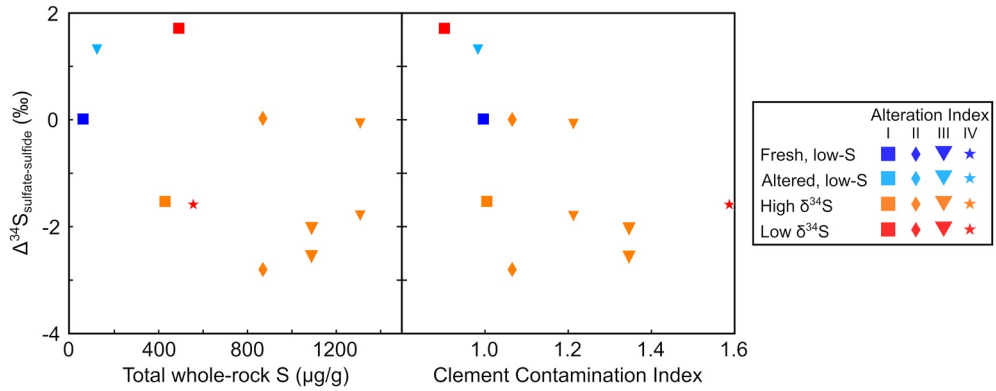

Figure 10. $\Delta^{34}S_{insoluble\ sulfate-sulfide}$ (‰) versus (a) total whole-rock S (µg/g) and (b) Clement (1982) contamination index in the Kimberley kimberlites.

The formation of sulfates requires prevailing relatively oxidising conditions in the later stage of kimberlite melt crystallisation and/or during subsolidus hydrothermal alteration. Previous work has indeed demonstrated that kimberlite melt oxygen fugacity progressively increases during crystallisation, based on experimental (e.g., Foley et al., 2019) as well as natural evidence, such as decreasing V/Sc in magmatic olivine rims (Giuliani, 2018; Howarth & Taylor, 2016); increasing melt Mg/Fe^{2+} during groundmass crystallisation (Bussweiler et al., 2015; Soltys et al., 2018a; Soltys, Giuliani, Phillips, & Kamenetsky, 2020); and increasing $Fe^{3+}/\Sigma Fe$ in garnet in peridotite xenoliths in kimberlites occurring shortly before kimberlite emplacement (Hanger et al., 2015). The formation of native Ni and Cu locally associated with other products of sulfide alteration does not contradict this scenario because these phases form under relatively oxidising conditions (i.e., log (fO_2) > quartz-fayalite-magnetite buffer). Although we recognize that the proposed scenario involves some caveats, we believe that this hypothesis represents the most parsimonious explanation for the puzzling observation that bulk-sulfide and -sulfate fractions in the Kimberley kimberlites have broadly similar $\delta^{34}S$ values. The lack of systematic differences (i.e., outside of analytical uncertainty) in $\Delta^{33}S$ between sulfides and sulfates in the examined samples (Table 2) does not preclude this hypothesis.

6.2. Sulfur Isotope Fractionation During Kimberlite Ascent and Emplacement

The variability of compositions in sulfide fractions from this study is unlikely to be representative of the S isotopic composition of the source of the Kimberley kimberlites, given the abundant petrographic evidence of hydrothermal alteration and modification of magmatic sulfides, and also the restricted range in Sr-Nd-Hf isotopes shown by these kimberlites (e.g., bulk-rock $\varepsilon Nd_i = -0.3$ to $+2.2$; perovskite $^{87}Sr/^{86}Sr_i = 0.70434$–$0.70478$; Giuliani et al., 2021; le Roex et al., 2003; Woodhead et al., 2009, 2019). This section discusses the potential processes that may have caused the wide S isotopic variability in the examined samples. Given the overall similarity between bulk-sulfide and bulk-sulfate S isotope compositions, for simplicity the discussion below is limited to the interpretation of bulk-sulfide S isotope ratios. In the following sections, processes that might have caused the variations observed in this study are considered in order of decreasing depth at which they might have occurred.

6.2.1. Entrainment and Assimilation of Lithospheric Mantle

Hypabyssal kimberlites contain a significant amount of mantle debris (e.g., Mitchell, 1986; Mitchell et al., 2019) mostly as xenocrystic cores of olivine grains (roughly between 20-30 vol.% of macrocrystic samples, but considerably less in aphanitic samples; Giuliani, 2018 and references therein). Such estimates for xenocrystic material in kimberlites are also in line with PGE patterns in kimberlites (Maier et al., 2017; Tappe, Stracke, et al., 2020). These olivine xenocrysts may contain inclusions of sulfides (e.g., Griffin et al., 2002). Several studies have also demonstrated that kimberlite melts react with and assimilate lithospheric mantle material during ascent (e.g., Bussweiler et al., 2016; Giuliani et al., 2020; Hunter & Taylor, 1982; Tovey et al., 2021). However, estimating the effects of entrainment and assimilation of lithospheric mantle material on S content and isotopic composition is difficult, owing to the low and variable S

contents in lithospheric mantle rocks beneath the Kimberley area (62–219 μg/g; Lorand & Grégoire, 2006). Such values are similar to the sulfur contents in the low-sulfur kimberlites from this study (<130 μg/g), and much lower than the highest (reduced) sulfur contents in silicate-carbonate melts at mantle depths (i.e., experimentally determined sulfur solubility of ~2,000–3,000 μg/g; Chowdhury & Dasgupta, 2020). Mantle assimilation can be modeled using a primitive kimberlite melt composition of between 40 and 680 μg/g S (this study, Becker & le Roex, 2006), and assuming asthenospheric $\delta^{34}S$ values (−1.3 ± 0.3‰; Labidi et al., 2013) in the primitive melt. This $\delta^{34}S$ value is in the range of sulfides from the Udachnaya-East kimberlite in Siberia (−2.8 to +2.2‰; Kitayama et al., 2017, Figure 1), which lacks evidence of crustal recycling in its deep mantle source based on supra-chondritic Nd-Hf isotopes (i.e., εNd_i = +3.4 to +5.7; εHf_i = +2.9 to +4.6; Carlson et al., 2006; Woodhead et al., 2019), and might be considered representative of the S isotope signature of the common PREMA-like source of kimberlites globally (Giuliani et al., 2021). Assimilation of 10% lithospheric mantle material (see Giuliani et al., 2020; Soltys et al., 2018b) with an assumed range in $\delta^{34}S$ values of −6 to +7‰ (Chaussidon & Lorand, 1990; Chaussidon et al., 1989; Giuliani et al., 2016; Tsai et al., 1979) results in a maximum range in melt composition of 60–635 μg/g S, and $\delta^{34}S$ values between −3.3 and + 2.0‰. Assimilation of mantle eclogites could generate larger variability because eclogitic sulfides extend to both lighter and heavier S isotope compositions compared to peridotitic sulfides (Chaussidon et al., 1989; Farquhar et al., 2002; Rudnick et al., 1993; Thomassot et al., 2009; Tsai et al., 1979). However, eclogites are poorly represented in the populations of mantle xenoliths (Jacob et al., 2009) and diamond inclusions (typically <5%; Phillips et al., 2004) derived from the Kimberley kimberlites, which makes assimilation of abundant eclogite unlikely in these kimberlites. Adding ~20% of entrained lithospheric mantle material would further shift the calculated range in S isotope values (−4.1 to +3.6‰), but not match the ranges found in the overall sample set of kimberlites from this study (−13 to +14‰), nor would it replicate the more limited range of compositions in low-sulfur kimberlites in the Kimberley area (−5.7 to +1.1‰; Figure 7; Table 2). We conclude that entrainment and assimilation of lithospheric mantle material does not play a very significant role in altering S-$\delta^{34}S$ systematics in kimberlites. This conclusion is in line with the low S contents of the lithospheric mantle beneath cratonic regions (Giuliani et al., 2016; Holwell et al., 2019; Lorand & Grégoire, 2006).

6.2.2. Degassing/Fluid Exsolution

The experiments conducted by Woodland et al. (2019) indicate that 200–1,000 μg/g S can be dissolved in silicate-carbonate melts at pressures of 5.0–10.5 GPa and temperatures of 1,400–1,600°C in melts containing 1–10 wt.% FeO. Similarly, 2,000–4,700 μg/g sulfur can be dissolved in a silicate-carbonate melt at 2.5–6.0 GPa and between 1,350–1,650°C on a nickel-free basis, decreasing slightly to 1,200–3,100 μg/g S when nickel is present (3–6 GPa; 1,400–1,650°C Chowdhury & Dasgupta, 2020). These melt compositions and melting conditions are appropriate for primary kimberlite melts (Soltys et al., 2018b; Stamm & Schmidt, 2017; and references therein). Becker and le Roex (2006) estimated a sulfur content of ~680 ± 600 μg/g in close-to-primary kimberlite melt compositions, which is within the limits of sulfur solubility in silicate-carbonate melts at high pressure and temperature, but much higher than whole-rock S contents in most of the samples in this study (see Table 2). It seems therefore likely that large amounts of sulfur were lost by the Kimberley kimberlites via fluid exsolution and degassing, which are prominent processes during kimberlite ascent and emplacement (e.g., Russell et al., 2012).

Muramatsu (1983) suggested that positive $\delta^{34}S$ values (up to ~+10‰) in the Kimberley kimberlites might be the result of degassing and preferential retention of heavier S isotopes in the residual magma. This assumption has been shown to be valid theoretically (Marini et al., 2011) and experimentally for silicate melts (Fiege et al., 2015) as well as in natural komatiite systems (Caruso et al., 2017) if S degassing occurs under strongly oxidising conditions (i.e., log (fO_2) ≥ QFM+2). However, the oxidation state of kimberlite magmas during ascent and related fluid exsolution, that is, before late-stage oxidation (see Section 6.1), might be relatively reduced (log (fO_2) ~ QFM-3 to QFM+2 based on olivine-spinel equilibrium: Fedortchouk & Canil, 2004; Zhu et al., 2021). This suggests that sulfur would likely be lost as H_2S rather than SO_2 in exsolved fluids, a process which decreases $\delta^{34}S$ in the residual melt (Marini et al., 2011). To understand if the restricted range of S isotope compositions shown by low-S kimberlites in this study (Figures 7 and 8) can be attributed to exsolution of a H_2S-bearing fluid (under equilibrium conditions), we have developed a quantitative model that describes the change in S content and isotopic composition of kimberlite melts after fluid exsolution. In this model, we have assumed a starting melt $\delta^{34}S$ of −1.3‰, which is representative

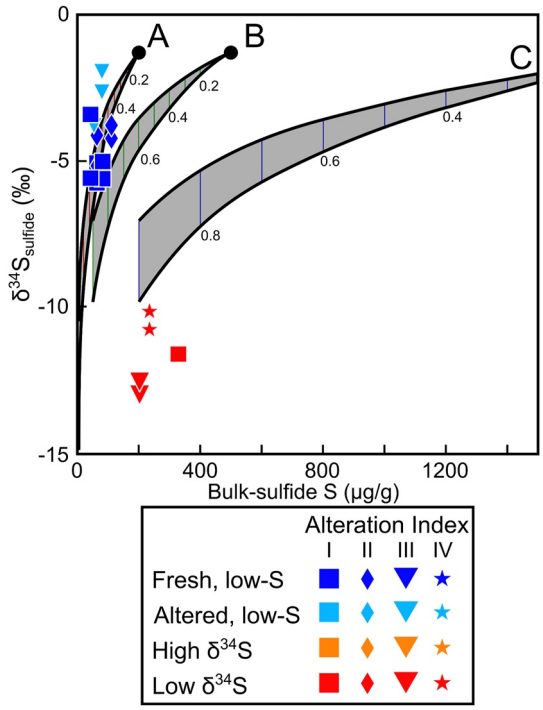

Figure 11. Rayleigh distillation model of sulfide exsolution and its effects on $\delta^{34}S_{sulfide}$ (‰) versus total whole-rock S (µg/g). Gray fields show model trajectories if starting melts contain (a) 200 µg/g, (b) 500 µg/g, and (c) 2,000 µg/g S, with a starting $\delta^{34}S$ of −1.3‰. Upper and lower bounds of the models represent $\alpha_{f\text{-}m}$ of 1.0025 and 1.0037, respectively; numbers next to fields represent fraction of fluid lost, and colored vertical lines represent 10% increments of fluid loss.

of the asthenospheric mantle (Labidi et al., 2013), and varied the S content in the initial melt between ~2,000 µg/g (i.e., maximum solubility of reduced S in silicate-carbonate melts similar to kimberlites; Chowdhury & Dasgupta, 2020) and 200 µg/g (i.e., marginally higher than the range of total S contents shown by the low-sulfur kimberlites in this study). The model assumes fractionation via Rayleigh distillation and employs the fluid/(silicate) melt fractionation factors of Fiege et al. (2015) for log (fO_2) ≤ QFM: $\alpha_{f\text{-}m}$ = 1.0025 at 1,200°C and 1.0037 at 1,000°C. Figure 11 shows that the limited spread in $\delta^{34}S$ of the low-S kimberlite samples can be reproduced if between 45% and 85% of sulfur is lost as H_2S (i.e., S^{2-}) via fluid exsolution from a similarly reduced, S-poor (200 µg/g) primitive melt. Employing S contents of 500 µg/g or higher in the primitive melt, it is not possible to match the isotopic composition of these low-S samples. Notably, if Rayleigh distillation is modeled assuming degassing under strongly oxidising conditions (log (fO_2) ~ QFM + 4 with S predominantly as S^{6+}; $\alpha_{f\text{-}m}$ = 0.9981 at 1,200°: Fiege et al., 2015), the melt $\delta^{34}S$ gradually increases as the fluid exsolves, which is the opposite of what is shown in Figure 11. Kinetic fractionation associated with non-equilibrium degassing would partition the lighter S isotopes in the gas phase regardless of fO_2 conditions, thus producing higher $\delta^{34}S$ values in the residual melt phase. This is the opposite of what is observed in the low-S kimberlites in this study which generally have $\delta^{34}S$ values lower than typical asthenospheric compositions (Figure 7; Labidi et al., 2013; Kitayama et al., 2017).

These results together permit some contribution from degassing and/or fluid exsolution under reducing conditions toward S isotope variability in the low-S samples from Kimberley. However, the lack of a consistent relationship between S-$\delta^{34}S$ across the whole data set make it unlikely that degassing is a major factor controlling S isotopic fractionation in the Kimberley kimberlites. Degassing under oxidising conditions, or at non-equilibrium, can effectively be ruled out based on the Rayleigh distillation models.

6.2.3. Crustal Contamination

Crustal contamination is a common phenomenon that affects kimberlites upon emplacement (e.g., Kjarsgaard et al., 2009; Mitchell, 1986, 2008) and entails both entrainment and assimilation of crustal material and infiltration by crustal-derived fluids. Crustal contamination can be clearly seen in the elevated bulk-rock Sr isotope compositions of kimberlites worldwide, relative to those in a magmatic phase that is robust against alteration such as perovskite (e.g., Heaman, 1989; Paton et al., 2007). Similarly, carbonate C-O isotopes of kimberlite rocks may display evidence for crustal contamination (e.g., Castillo-Oliver et al., 2020; Giuliani, Phillips, Kamenetsky, Fiorentini, et al., 2014). The work of le Roex et al. (2003) identified some major and trace element proxies that may be helpful in identifying crustal contamination in kimberlite magmas (e.g., SiO_2 vs. MgO; Gd/Lu vs. SiO_2; Figure 6), in addition to the contamination index of Clement (1982). The major element compositions of kimberlites from this study do not show any signs of significant crustal contamination using these screens, with samples K-1, P-3 and E310A being the only notable exceptions due to their higher SiO_2 contents (relative to MgO; Figure 6a). It is thus important to investigate the possible impact of crustal contamination on the S contents and isotope compositions of these kimberlites, but also the other samples for which crustal contamination is not apparent based on major and trace element geochemistry.

Maruoka et al. (2003) examined South African sedimentary rocks from the Permian-Triassic transition that crop out around the Kimberley area, and found high S contents (up to 3.2 wt.%) and variable $\delta^{34}S$ (−11.4 to +12.9‰; Figure 2). A similar organic-rich shale from the Whitehill Formation, which overlies the Dwyka Group, was analyzed by Faure and Cole (1999) and returned similar S contents (0.4–2.1 wt.% S) and a smaller range of predominantly positive $\delta^{34}S$ values (−0.3 to +6.9‰). Finally, some sulfur isotope data have

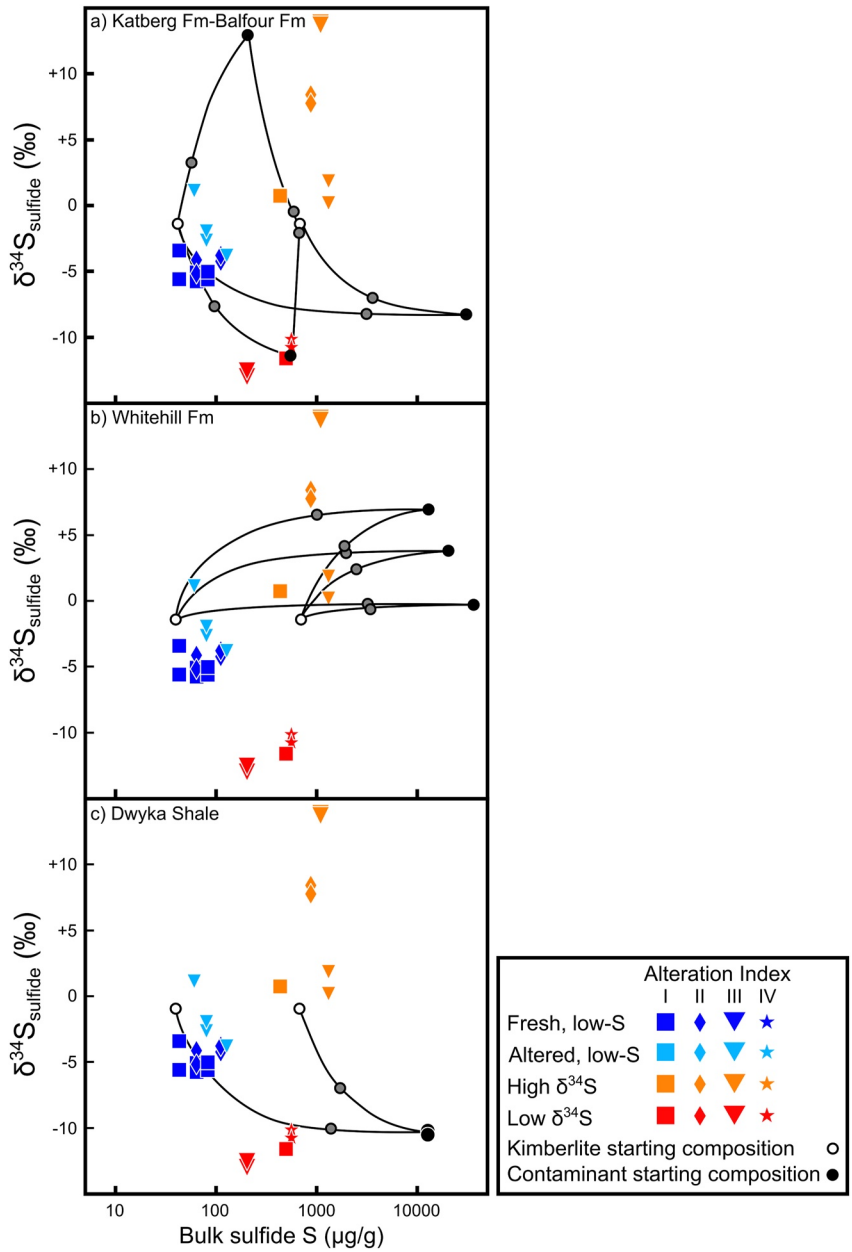

Figure 12. Mixing model trajectories (black lines) in S-δ^{34}S space between kimberlite (open circles) and country rocks (black circles) including the (a) Katberg/Balfour formations (Maruoka et al., 2003), (b) Whitehill formation (Faure & Cole, 1999), and (c) Dwyka shale (this study); data from this study displayed with same symbols as in Figure 8; gray circles represent mixing of 90% kimberlite + 10% country rock contaminant.

been collected for galena and sphalerite in the Ventersdorp lavas, yielding a limited range of δ^{34}S from −6.3 to −3.4‰ (Whitelaw et al., 2005, Figure 2c). These studies demonstrate that the country rocks local to the Kimberley kimberlites are not homogeneous in terms of their δ^{34}S values.

The data for these country rocks can be used to model crustal contamination of the Kimberley kimberlites, for which we assume a primitive melt composition of 40–680 µg/g S (this study; Becker & le Roex, 2006) and asthenospheric δ^{34}S values (−1.3 ± 0.3‰; Labidi et al., 2013), as used in the previous model of lithospheric mantle assimilation. Figure 12 displays the results of these mixing models. Three samples of the Kimberley kimberlites (BHK-1, E310F, E310A: "high-sulfur negative-δ^{34}S samples") have moderately high S concentrations (e.g., total S up to 560 µg/g) and their bulk-sulfide δ^{34}S values are very negative (−10.1

to −13.0‰; Table 2; Figures 7 and 8). These samples contain sphalerite (±galena) as one of the dominant sulfide components (Table 1). Sphalerite is atypical of kimberlites, wherein Cu-Fe-Ni-bearing minerals such as chalcopyrite and pentlandite are more common primary magmatic sulfides (e.g., Mitchell, 1986; Giuliani, Phillips, Kamenetsky, Fiorentini, et al., 2014). For example, the unusually heavy S isotope compositions ($\delta^{34}S > +14‰$) of galena and sphalerite in Yakutian kimberlites (Vinogradov & Ilupin, 1972) indicate a likely crustal origin for these phases (Giuliani, Phillips, Kamenetsky, Fiorentini, et al., 2014). The occurrence of sphalerite (±galena) and moderately high bulk-sulfide concentrations can be probably linked to crustal contamination by xenocrystic crustal sulfides or S-bearing fluids sourced in country rocks such as the Dwyka shales, a hypothesis consistent with the similar highly negative $\delta^{34}S$ values of these shales (−10.5 to −10.2‰) and the high-sulfur negative-$\delta^{34}S$ kimberlite samples (Figure 7; Table 2). Although direct assimilation of Dwyka shale into these samples might be feasible based on the mass balance derived from the mixing model (i.e., <10%; Figure 12c), samples E310F and E310 from the Eyebrow dyke come from a significantly deeper (720 m level) of the former De Beers mine than the Dwyka shales, which only extend to ~90 m of depth from the mine surface (Clement et al., 1986). The samples from the Eyebrow dyke were emplaced into the Ventersdorp lavas (Clement et al., 1986, Figure 2). This observation rules out crustal contamination by addition of country-rock sulfides or bulk shale assimilation, and rather suggests introduction of shale-derived sulfur via hydrothermal fluids. We note that a fresh sample (E310F, alteration index I) is included in this group of high-sulfur negative-$\delta^{34}S$ samples, which indicates that hydrothermal fluids can introduce crustal sulfur and hence overprint the primary S isotope signatures also in kimberlites that are apparently very fresh. Similarly, only one of these three samples (E310A) shows geochemical evidence of crustal contamination (Figure 6), showing that S isotopes may be more sensitive to crustal contamination than other geochemical proxies.

The other four S-rich kimberlites (K-1, P-3, WA-1 and WFSC-5: "high-sulfur positive-$\delta^{34}S$ samples") exhibit highly variable and positive bulk-sulfide $\delta^{34}S$ (+0.2 to +13.9‰; Table 2; Figures 7 and 8). Petrographic observations by optical and scanning-electron microscopy indicates that galena is a major sulfide phase in samples P-3 and WFSC-5 ($\delta^{34}S = +7.8$ to +13.9‰). In kimberlite WA-1, galena and pyrite, both minerals that are atypical in kimberlites, occur together with more abundant but altered Ni-Fe-Cu sulfides, whereas in sample K-1 pyrite is the major sulfide phase (Figure 3f). These two S-rich samples have lighter $\delta^{34}S$ of between +0.2 and +1.9‰ (Table 2). While a common origin of sulfur in the high-sulfur positive-$\delta^{34}S$ samples is probably unlikely, the occurrence of dominant crustal sulfides (galena and pyrite) and enrichment in sulfur (total S up to 1,312 μg/g; Table 2) are consistent with a prevalent crustal derivation of S in these kimberlites. Assimilation of or interaction with fluids derived from the Katberg, Balfour or Whitehill Formations might explain some of the S isotope variability to positive $\delta^{34}S$ values found in these kimberlites (Figures 12a and 12b), whereas the elevated S concentrations could be attributed to a combination of crustal contamination and, in part, extensive magmatic differentiation (see the low SiO_2 and MgO contents in the sill samples K-1 and P-3; Figure 5; Data Set S1). As for the high-sulfur negative-$\delta^{34}S$ samples, there is no clear link between S isotope composition and extent of groundmass alteration (i.e., alteration index between I and III in the high-sulfur positive-$\delta^{34}S$ samples; Table 2; Figures 7 and 8) or other geochemical indices of crustal contamination (i.e., high SiO_2/MgO only in K-1 and P-3; Figure 6a).

In summary, the variability in the S isotopic composition of the high-S kimberlites from this study probably reflects varying amounts of interaction with crustal fluids sourced from country rocks featuring highly variable S isotope systematics, which introduced sulfides that are unusual in kimberlites, including sphalerite, galena and pyrite. The mixing models in Figure 12 also suggest that the $\delta^{34}S$ values of low-S fresh and low-S altered kimberlites could be partly reproduced by admixing of relatively small proportions (<10%) of S from the country rocks of the Katberg and Balfour Formations or from the Dwyka shale, but only if the starting melt S content was toward the lower end of the range utilized in the model (i.e., ~40 μg/g). However, unlike the samples that contain high concentrations of S, the sulfides in low-S kimberlite samples tend to be typical of the kimberlite assemblage (e.g., pentlandite, chalcopyrite) and are optically fresh. These samples also display no (fresh) or little (altered) geochemical evidence of crustal contamination. Consequently, it seems unlikely that this signature is related to crustal over-printing, and this possibility is examined in the following section.

6.3. Fingerprinting the Source of Sulfur in the Kimberley Kimberlites

The dominant sulfide phases in the low-S kimberlites are Ni-Fe-Cu sulfides (pentlandite and chalcopyrite); conversely, sulfides that are exotic in kimberlites, such as galena, are absent. These kimberlites feature a relatively large range in $\delta^{34}S$ values (−5.7 to +1.1‰), which narrows down to between −5.7 and −3.4‰ once only the five "low-S fresh samples" (alteration index I and II) are considered (Figures 7 and 8; Table 2). We do not have a straightforward explanation as to why two of the three "low-S partially altered samples" (alteration index III) exhibit isotopically heavier S isotopes (−2.6 to +1.1‰; Figure 7; Table 2). A possible interpretation is that magmatic sulfur was partly replaced by crustal sulfur, which would be consistent with the low S contents and common replacement of magmatic Ni-Fe-Cu sulfides by secondary Ni or Cu sulfides (plus native metals and magnetite; Table 1) in these samples. Alternatively, kinetic fractionation associated with partial oxidation of sulfides could increase $\delta^{34}S$ in the residual sulfides. This process was previously proposed by Giuliani et al. (2016) to explain a direct correlation between the amount of S lost during sulfide alteration associated with serpentinization, and the deviation of bulk-sulfide $\delta^{34}S$ from the average of in-situ sulfide $\delta^{34}S$ in mantle peridotites. Under equilibrium conditions, sulfate produced during partial oxidation of sulfides preferentially incorporates heavy S, leaving residual sulfides enriched in lighter isotopes. However, experimental work has shown that the opposite is true if kinetic fractionation occurs during oxidation (Fry et al., 1988; Grinenko & Mineyev, 1992), and this process has been documented in oceanic peridotites (Alt & Shanks, 2011; Delacour et al., 2008). As outlined in Section 6.1, this process could have also played a role in determining the large isotopic disequilibrium recorded by bulk-sulfide and bulk-sulfate fractions in the Kimberlite kimberlites.

The low S contents (bulk-sulfide $S < 111$ μg/g) and narrow range in $\delta^{34}S$ (−5.7 to −3.4‰; Figures 7 and 8; Table 2) in the "low-S fresh samples" cannot be explained by S loss during fluid exsolution or degassing as outlined in Section 6.2.3. Likewise, the dominance of fresh magmatic Ni-Fe-Cu sulfides in these samples makes it unlikely that the S isotopic compositions of these kimberlites were affected by crustal contamination or entrainment of lithospheric mantle material. Assimilation of S-bearing lithospheric peridotites will generate S isotope compositions as low as ∼−3‰ assuming a typical asthenospheric source of S in the kimberlites ($\delta^{34}S = -1.3$‰; Labidi et al., 2013) and using available constraints for sulfur isotopes in mantle sulfides (see Section 6.2.1). The final question is: what could generate this shift toward light S isotope compositions in the low-S fresh samples of the Kimberley kimberlites?

The $\delta^{34}S$ range of −5.7 to −3.4‰ is remarkably similar to that of sulfides in mantle polymict breccias from Kimberley (−5.4 to −1.0‰: Giuliani et al., 2016), which are considered to be the crystallisation products of kimberlite melts that have stalled in the lithosphere (Giuliani, Phillips, Kamenetsky, Kendrick, et al., 2014; Lawless et al., 1979; Zhang et al., 2000). These compositions extend to significantly lower values than those expected for the asthenospheric mantle source of mid-ocean ridge basalts (−1.3 ± 0.3‰; Labidi et al., 2013) and also to lower values than sulfides in the Udachnaya-East kimberlite (−2.8 to +2.2‰; Kitayama et al., 2017, Figure 1). Assuming no isotopic fractionation between melt and residual mantle source (Marini et al., 2011; Ohmoto & Rye, 1979), and having addressed the effects of lithospheric mantle assimilation, degassing, crustal contamination and sulfide alteration upon $\delta^{34}S$, the most straightforward explanation for the light S isotope composition of the Kimberley kimberlites is the presence of a recycled S component within their mantle source. Incorporation of low temperature-altered oceanic crust (∼−6‰; Alt & Shanks, 2011, Figure 1) into a deep-mantle source could explain the isotopic compositions of magmatic sulfides in the Kimberley kimberlites. However, a simple mass balance calculation indicates that a very high quantity of altered oceanic crust (∼75%; 940 μg/g S; Alt & Shanks, 2011) would have to be added to a mantle source containing 206 μg/g S (Sun et al., 2020) to explain the lowest value in the fresh samples from this study (−5.7‰ $\delta^{34}S$). This is not consistent with mass balance calculations based on other isotopic systems, including Nd, Hf (e.g., Tappe et al., 2013; Woodhead et al., 2019), and oxygen (Giuliani et al., 2019). The variations observed in sedimentary pyrite (average values −25 to +25‰; Farquhar et al., 2010) mean that a fluid that incorporated sulfur from a S-rich sedimentary component with very low $\delta^{34}S$ might be a more likely candidate for the recycled signature, provided other isotopic (e.g., Pb, Os) criteria, for which insufficient constraints are available, can be met.

The presence of mass-independent-fractionated (MIF) S in one of the freshest kimberlites from Kimberley (BK-1: $\delta^{34}S = -5.3$‰; $\Delta^{33}S = -0.059$‰; $\Delta^{36}S = +0.162$‰; $n = 2$) might suggest a potentially ancient

(pre-2.4 Ga) origin of sulfur in this sample (e.g., Farquhar & Wing, 2003) or some contribution from sulfur that was biologically processed at low temperature by microbes (Farquhar et al., 2003; Johnston et al., 2005). However, the lack of significant non-zero $\Delta^{33}S$ in the other four low-S fresh kimberlites and its occurrence in samples (BHK-1, WFSC-5 and P-3) that were probably affected by crustal contamination does not allow us to utilize $\Delta^{33}S$ to make any robust inference about the origin of sulfur in the Kimberley kimberlites.

As discussed by Woodhead et al. (2019), the steep Nd or Hf isotope versus time trend shown by Mesozoic (~180–70 Ma) kimberlites in southern Africa, including Kimberley, might relate to either radiogenic ingrowth in a source with unusually high Sm/Nd and Lu/Hf, or to the presence of a recycled crustal component with low $^{143}Nd/^{144}Nd$ and $^{176}Hf/^{177}Hf$ in their mantle source. Resolving this question is important because kimberlites emplaced since 200 Ma in southern Africa and other large kimberlite provinces (Brazil, western Canada) display initial $^{143}Nd/^{144}Nd$ and $^{176}Hf/^{177}Hf$ ratios that reach significantly lower (i.e., sub-chondritic) values compared to older kimberlites, which could be attributed to crustal recycling (e.g., Tappe et al., 2013; Tovey et al., 2021). The new S isotopic data presented herein support the hypothesis that a deeply recycled crustal component has played a role in the genesis of the ~90 Ma Kimberley kimberlites and, by extension, the other Cretaceous southern African kimberlites, which display similar Sr-Nd-Hf isotope systematics (Giuliani et al., 2021). Further support for this idea can be found in previously published Sr isotopic data for perovskite in the Kimberley kimberlites (Woodhead et al., 2009), which have more radiogenic initial $^{87}Sr/^{86}Sr$ ratios (~0.7045) than coeval kimberlites, such as those in Botswana (0.703–0.704), or in HIMU-like initial $^{206}Pb/^{204}Pb$ ratios in the Kimberley kimberlites (Collerson et al., 2010; Kramers, 1977; Smith, 1983). This change in composition in young kimberlites might support recent speculation by Woodhead et al. (2019) of abrupt incorporation of subducted material from a slab "graveyard" into the PREMA-like mantle source of kimberlites globally (see Giuliani et al., 2021). Alternatively, interaction between mantle plumes and subducted material in the mantle transition zone (Nowell et al., 2004; Pearson et al., 2019; Tappe et al., 2013) may also explain the compositional features of the Kimberley kimberlites. Although it is not possible to give a definitive answer as to which of these mechanisms is most likely, it is becoming clearer that young (<200 Ma) kimberlites must have incorporated some recycled material into their source region at some stage during their genesis. Further investigation of S isotopes as a proxy for subducted material in young (<200 Ma) and old (>200 Ma) fresh kimberlites might improve the strength of this conclusion while also testing any potential cycling of crustal material into the deep source of kimberlites before 200 Ma.

7. Conclusions

This study presents sulfide and sulfate petrography, S compositional and isotopic characteristics of hypabyssal kimberlites from the Kimberley cluster and demonstrates the use of S isotope geochemistry as a petrogenetic tool for kimberlite rocks. Although the data presented herein show a wide range in bulk-sulfide S isotopic compositions ($\delta^{34}S$ from −13 to +14‰) with no simple correlation with emplacement style, alteration conditions or geochemical indicators of crustal contamination, this range can be broken down into four distinct groups. Two groups of S-rich kimberlites were locally contaminated by S-bearing crustal fluids from different country rocks, which introduced exotic sulfide phases (e.g., sphalerite and galena) combined with either isotopically light ($\delta^{34}S < -10$‰) or heavy ($\delta^{34}S > 0$‰) sulfur. Once a group of partially altered samples is excluded from the low-S samples which only contain magmatic Ni-Fe-Cu sulfides, the remaining kimberlites display a much more limited range in $\delta^{34}S$ values (−5.7 to −3.4‰). These isotopic compositions cannot be reproduced by lithospheric mantle assimilation or fluid loss during melt ascent and emplacement assuming a kimberlite source with S isotope characteristics typical of (MORB-like) asthenospheric mantle. The S isotopic compositions of the Kimberley kimberlites require a contribution from an isotopically light S component which is probably represented by deeply recycled crustal material of sedimentary origin. This inference is supported by recent radiogenic isotope studies that indicate a possible change in kimberlite source components in southern Africa after around 200 Ma, although the cause of this disruption remains unclear. This study suggests that the combination of detailed sulfide petrography and S isotope geochemistry in fresh kimberlite rocks can provide important insights into the occurrence and origin of deeply subducted material in the source of kimberlites, thus providing a further tool to investigate mantle chemical geodynamics through time.

Data Availability Statement

In line with the policies of AGU Journals, the data used in this study have been made publicly available in the ETH Zürich Research Collection at https://doi.org/10.3929/ethz-b-000501238.

Acknowledgments
The authors thank Graham Hutchinson for his maintenance of SEM facilities at the University of Melbourne. We thank De Beers Consolidated Mines, the University of Cape Town, Petra Diamonds and Simon Shee for contributing samples for this work, as well as Jock Robey for his assistance during fieldwork and sample collection in the Kimberley region. We also thank Hayden Dalton for sharing with us his enormous dataset compiling published kimberlite geochemical data. This work was funded by the Ambizione fellowship awarded to A. Giuliani by the Swiss National Science Foundation (grant no. PZ00P2_180126/1). We are grateful to Sebastian Tappe, Graham Pearson, and Jabrane Labidi for their constructive comments, and for the editorial handling of Janne Blichert-Toft. Reviews of a previous version of this manuscript by Crystal LaFlamme, Emilie Thomassot and Nick Arndt helped to improve and clarify the contents of this work.

References

Abersteiner, A., Kamenetsky, V. S., Goemann, K., Giuliani, A., Howarth, G. H., Castillo-Oliver, M., et al. (2019). Composition and emplacement of the Benfontein kimberlite sill complex (Kimberley, South Africa): Textural, petrographic and melt inclusion constraints. *Lithos*, *324–325*, 297–314. https://doi.org/10.1016/j.lithos.2018.11.017

Alt, J. C. (1995). Sulfur isotopic profile through the oceanic crust: Sulfur mobility and seawater-crustal sulfur exchange during hydrothermal alteration. *Geology*, *23*(7), 585–588. https://doi.org/10.1130/0091-7613(1995)023<0585:siptto>2.3.co;2

Alt, J. C., & Shanks, W. C. (2011). Microbial sulfate reduction and the sulfur budget for a complete section of altered oceanic basalts, IODP Hole 1256D (eastern Pacific). *Earth and Planetary Science Letters*, *310*, 73–83. https://doi.org/10.1016/j.epsl.2011.07.027

Arnold, G. L., Brunner, B., Müller, I. A., & Roy, H. (2014). Modern applications for a total sulfur reduction distillation method—What's old is new again. *Geochemical Transactions*, *15*. https://doi.org/10.1186/1467-4866-15-4

Aubaud, C., Pineau, F., Hékinian, R., & Javoy, M. (2006). Carbon and hydrogen isotope constraints on degassing of CO_2 and H_2O in submarine lavas from the Pitcairn hotspot (South Pacific). *Geophysical Research Letters*, *33*(2). https://doi.org/10.1029/2005gl024907

Batumike, J. M., Griffin, W. L., Belousova, E. A., Pearson, N. J., O'Reilly, S. Y., & Shee, S. R. (2008). LAM-ICPMS U-Pb dating of kimberlitic perovskite: Eocene-Oligocene kimberlites from the Kundelungu Plateau, DR Congo. *Earth and Planetary Science Letters*, *267*, 609–619. https://doi.org/10.1016/j.epsl.2007.12.013

Becker, M., & le Roex, A. P. (2006). Geochemistry of South African on- and off-craton, Group I and Group II kimberlites: Petrogenesis and source region evolution. *Journal of Petrology*, *47*(4), 673–703. https://doi.org/10.1093/petrology/egi089

Beunon, H., Mattielli, N., Doucet, L. S., Moine, B., & Debret, B. (2020). Mantle heterogeneity through Zn systematics in oceanic basalts: Evidence for a deep carbon cycling. *Earth-Science Reviews*, 103174. https://doi.org/10.1016/j.earscirev.2020.103174

Bigeleisen, J., & Mayer, M. G. (1947). Calculation of equilibrium constants for isotopic exchange reactions. *Journal of Chemical Physics*, *15*, 261–267. https://doi.org/10.1063/1.1746492

Bussweiler, Y., Foley, S. F., Prelevic, D., & Jacob, D. E. (2015). The olivine macrocryst problem: New insights from minor and trace element compositions of olivine from Lac de Gras kimberlites, Canada. *Lithos*, *220–223*, 238–252. https://doi.org/10.1016/j.lithos.2015.02.016

Bussweiler, Y., Stone, R. S., Pearson, D. G., Luth, R. W., Stachel, T., Kjarsgaard, B. A., & Menzies, A. (2016). The evolution of calcite-bearing kimberlites by melt-rock reaction: Evidence from polymineralic inclusions within clinopyroxene and garnet megacrysts from Lac de Gras kimberlites, Canada. *Contributions to Mineralogy and Petrology*, *171*(7), 65. https://doi.org/10.1007/s00410-016-1275-3

Canfield, D. E., Raiswell, R., Westrich, J. T., Reaves, C. M., & Berner, R. A. (1986). The use of chromium reduction in the analysis of reduced inorganic sulfur in sediments and shales. *Chemical Geology*, *54*, 149–155. https://doi.org/10.1016/0009-2541(86)90078-1

Carlson, R. W., Czamanske, G., Fedorenko, V., & Ilupin, I. (2006). A comparison of Siberian meimechites and kimberlites: Implications for the source of high-Mg alkalic magmas and flood basalts. *Geochemistry, Geophysics, Geosystems*, *7*(11). https://doi.org/10.1029/2006gc001342

Cartigny, P., Palot, M., Thomassot, E., & Harris, J. W. (2014). Diamond formation: A stable isotope perspective. *Annual Review of Earth and Planetary Sciences*, *42*, 699–732. https://doi.org/10.1146/annurev-earth-042711-105259

Caruso, S., Fiorentini, M. L., Moroni, M., & Martin, L. A. J. (2017). Evidence of magmatic degassing in Archean komatiites: Insights from the Wannaway nickel-sulfide deposit, Western Australia. *Earth and Planetary Science Letters*, *479*, 252–262. https://doi.org/10.1016/j.epsl.2017.09.035

Castillo-Oliver, M., Giuliani, A., Griffin, W. L., O'Reilly, S. Y., Drysdale, R. N., Abersteiner, A., et al. (2020). New constraints on the source, composition, and post-emplacement modification of kimberlites from in situ C-O-Sr-isotope analyses of carbonates from the Benfontein sills (South Africa). *Contributions to Mineralogy and Petrology*, *175*(4), 1–20. https://doi.org/10.1007/s00410-020-1662-7

Chaussidon, M., Albarède, F., & Sheppard, S. M. F. (1989). Sulfur isotope variations in the mantle from ion microprobe analyses of micro-sulfide inclusions. *Earth and Planetary Science Letters*, *92*, 144–156. https://doi.org/10.1016/0012-821x(89)90042-3

Chaussidon, M., & Lorand, J.-P. (1990). Sulphur isotopic composition of orogenic spinel lherzolite massifs from Ariege (North-Eastern Pyrenees, France): An ion microprobe study. *Geochimica et Cosmochimica Acta*, *54*, 2835–2846. https://doi.org/10.1016/0016-7037(90)90018-g

Choi, E., Fiorentini, M. L., Giuliani, A., Foley, S. F., Maas, R., & Taylor, W. R. (2020). Subduction-related petrogenesis of Late Archean calc-alkaline lamprophyres in the Yilgarn Craton (Western Australia). *Precambrian Research*, *338*, 105550. https://doi.org/10.1016/j.precamres.2019.105550

Chowdhury, P., & Dasgupta, R. (2020). Sulfur extraction via carbonated melts from sulfide-bearing mantle lithologies—Implications for deep sulfur cycle and mantle redox. *Geochimica et Cosmochimica Acta*, *269*, 376–397. https://doi.org/10.1016/j.gca.2019.11.002

Clement, C. R. (1982). A comparative geological study of some major kimberlite pipes in the Northern Cape and Orange Free State. PhD thesis. University of Cape.

Clement, C. R., Harris, J. W., Robinson, D. N., & Hawthorne, J. B. (1986). The de Beers kimberlite pipe: A historic South African diamond mine. In C. R. Anhauesser, & S. Maske (Eds.), *Mineral deposits of South Africa* (pp. 2193–2214). Geological Society of South Africa.

Collerson, K. D., Williams, Q., Ewart, A. E., & Murphy, D. T. (2010). Origin of HIMU and EM-1 domains sampled by ocean island basalts, kimberlites and carbonatites: The role of CO_2-fluxed lower mantle melting in thermochemical upwellings. *Physics of the Earth and Planetary Interiors*, *181*, 112–131. https://doi.org/10.1016/j.pepi.2010.05.008

Dalton, H., Giuliani, A., O'Brien, H., Phillips, D., Hergt, J., & Maas, R. (2019). Petrogenesis of a hybrid cluster of evolved kimberlites and ultramafic lamprophyres in the Kuusamo area, Finland. *Journal of Petrology*, *60*, 2025–2050. https://doi.org/10.1093/petrology/egz062

Dawson, J. B., & Hawthorne, J. B. (1973). Magmatic sedimentation and carbonatitic differentiation in kimberlite sills at Benfontein, South Africa. *Journal of the Geological Society of London*, *129*(1), 61–85. https://doi.org/10.1144/gsjgs.129.1.0061

Delacour, A., Früh-Green, G. L., Bernasconi, S. M., & Kelley, D. S. (2008). Sulfur in peridotites and gabbros at Lost City (30°N, MAR): Implications for hydrothermal alteration and microbial activity during serpentinization. *Geochimica et Cosmochimica Acta*, *72*, 5090–5110. https://doi.org/10.1016/j.gca.2008.07.017

D'Eyrames, E., Thomassot, E., Kitayama, Y., Golovin, A., Korsakov, A., & Ionov, D. (2017). A mantle origin for sulfates in the unusual "salty" Udachnaya-East kimberlite from sulfur abundances, speciation and their relationship with groundmass carbonates. *Bulletin de la Societe Geologique de France*, *188*(1–2), 67–74. https://doi.org/10.1051/bsgf/2017007

Donaldson, C. H., & Reid, A. M. (1982). Multiple intrusion of a kimberlite dyke. *South African Journal of Geology*, *85*(1), 1–23. https://doi.org/10.1007/978-1-349-06242-3_1

Eggins, S. M., Woodhead, J. D., Kinsley, L. P. J., Mortimer, G. E., Sylvester, P., McCulloch, M. T., et al. (1997). A simple method for the precise determination of ≥40 trace elements in geological samples by ICPMS using enriched isotope internal standardisation. *Chemical Geology*, *134*, 311–326. https://doi.org/10.1016/s0009-2541(96)00100-3

Eiler, J. M. (2001). Oxygen isotope variations of basaltic lavas and upper mantle rocks. *Reviews in Mineralogy and Geochemistry*, *43*, 319–364. https://doi.org/10.2138/gsrmg.43.1.319

Eldridge, C. S., Compston, W., Williams, I. S., Harris, J. W., & Bristow, J. W. (1991). Isotope evidence for the involvement of recycled sediments in diamond formation. *Nature*, *353*, 649–653. https://doi.org/10.1038/353649a0

Farquhar, J., Johnston, D. T., Wing, B. A., Habicht, K. S., Canfield, D. E., Airieau, S., & Thiemens, M. H. (2003). Multiple sulfur isotopic interpretations of biosynthetic pathways: Implications for biological signatures in the sulphur isotope record. *Geobiology*, *1*(1), 27–36. https://doi.org/10.1046/j.1472-4669.2003.00007.x

Farquhar, J., & Wing, B. A. (2003). Multiple sulfur isotopes and the evolution of the atmosphere. *Earth and Planetary Science Letters*, *213*(1–2), 1–13. https://doi.org/10.1016/s0012-821x(03)00296-6

Farquhar, J., Wing, B. A., McKeegan, K. D., Harris, J. W., Cartigny, P., & Thiemens, M. H. (2002). Mass-independent sulfur of inclusions in diamond and sulfur recycling on early Earth. *Science*, *298*, 2369–2372. https://doi.org/10.1126/science.1078617

Farquhar, J., Wu, N., Canfield, D. E., & Oduro, H. (2010). Connections between sulfur cycle evolution, sulfur isotopes, sediments, and base metal sulfide deposits. *Economic Geology*, *105*, 509–533. https://doi.org/10.2113/gsecongeo.105.3.509

Faure, K., & Cole, D. (1999). Geochemical evidence for lacustrine microbial blooms in the vast Permian Main Karoo, Paraná, Falkland Islands and Huab basins of southwestern Gondwana. *Palaeogeography, Palaeoclimatology, Palaeoecology*, *152*, 189–213. https://doi.org/10.1016/s0031-0182(99)00062-0

Fedortchouk, Y., & Canil, D. (2004). Intensive variables in kimberlite magmas, Lac de Gras, Canada and implications for diamond survival. *Journal of Petrology*, *45*(9), 1725–1745. https://doi.org/10.1093/petrology/egh031

Fiege, A., Holtz, F., Behrens, H., Mandeville, C. W., Shimizu, N., Crede, L. S., & Göttlicher, J. (2015). Experimental investigation of the S and S-isotope distribution between H_2O-S ± Cl fluids and basaltic melts during decompression. *Chemical Geology*, *393–394*, 36–54. https://doi.org/10.1016/j.chemgeo.2014.11.012

Field, M., Stiefenhofer, J., Robey, J., & Kurszlaukis, S. (2008). Kimberlite-hosted diamond deposits of southern Africa: A review. *Ore Geology Reviews*, *34*, 33–75. https://doi.org/10.1016/j.oregeorev.2007.11.002

Fitzpayne, A., Giuliani, A., Harris, C., Thomassot, E., Cheng, C., & Hergt, J. (2019). Evidence for subduction-related signatures in the southern African lithosphere from the N-O isotopic composition of metasomatic mantle minerals. *Geochimica et Cosmochimica Acta*, *266*, 237–257. https://doi.org/10.1016/j.gca.2019.02.037

Fitzpayne, A., Giuliani, A., Hergt, J., Woodhead, J. D., & Maas, R. (2020). Isotopic analyses of clinopyroxenes demonstrate the effects of kimberlite melt metasomatism upon the lithospheric mantle. *Lithos*, *370–371*, 105595. https://doi.org/10.1016/j.lithos.2020.105595

Foley, S. F., Yaxley, G. M., & Kjarsgaard, B. A. (2019). Kimberlites from source to surface: Insights from experiments. *Elements*, *15*, 393–398. https://doi.org/10.2138/gselements.15.6.393

Fry, B., Ruf, W., Gest, H., & Hayes, J. M. (1988). Sulfur isotope effects associated with oxidation of sulfide by O_2 in aqueous solution. *Chemical Geology*, *73*, 205–210. https://doi.org/10.1016/0168-9622(88)90001-2

Geng, L., Savarino, J., Caillon, N., Gautier, E., Farquhar, J., Dottin, J. W., III, et al. (2019). Intercomparison measurements of two ^{33}S-enriched sulfur isotope standards. *Journal of Analytical and Atomic Spectroscopy*, *34*, 1263–1271. https://doi.org/10.1039/c8ja00451j

Giuliani, A. (2018). Insights into kimberlite petrogenesis and mantle metasomatism from a review of the compositional zoning of olivine in kimberlites worldwide. *Lithos*, *312–313*, 322–342. https://doi.org/10.1016/j.lithos.2018.04.029

Giuliani, A., Fiorentini, M. L., Martin, L. A., Farquhar, J., Phillips, D., Griffin, W. L., & LaFlamme, C. (2016). Sulfur isotope composition of metasomatised mantle xenoliths from the Bultfontein kimberlite (Kimberley, South Africa): Contribution from subducted sediments and the effect of sulfide alteration on S isotope systematics. *Earth and Planetary Science Letters*, *445*, 114–124. https://doi.org/10.1016/j.epsl.2016.04.005

Giuliani, A., Jackson, M. G., Fitzpayne, A., & Dalton, H. (2021). Remnants of early Earth differentiation in the deepest mantle-derived lavas. *Proceedings of the National Academy of Sciences*, *118*, e2015211118. https://doi.org/10.1073/pnas.2015211118

Giuliani, A., Martin, L. A. J., Soltys, A., & Griffin, W. L. (2019). Mantle-like oxygen isotopes in kimberlites determined by in situ SIMS analyses of zoned olivine. *Geochimica et Cosmochimica Acta*, *266*, 274–291. https://doi.org/10.1016/j.gca.2019.03.032

Giuliani, A., & Pearson, D. G. (2019). Kimberlites: From deep Earth to diamond mines. *Elements*, *15*, 377–380. https://doi.org/10.2138/gselements.15.6.377

Giuliani, A., Pearson, D. G., Soltys, A., Dalton, H., Phillips, D., Foley, S. F., et al. (2020). Kimberlite genesis from a common carbonate-rich primary melt modified by lithospheric mantle assimilation. *Science Advances*, *6*(17), eaaz0424. https://doi.org/10.1126/sciadv.aaz0424

Giuliani, A., Phillips, D., Kamenetsky, V. S., Fiorentini, M. L., Farquhar, J., & Kendrick, M. A. (2014). Stable isotope (C, O, S) compositions of volatile-rich minerals in kimberlites: A review. *Chemical Geology*, *374–375*, 61–83. https://doi.org/10.1016/j.chemgeo.2014.03.003

Giuliani, A., Phillips, D., Kamenetsky, V. S., Kendrick, M. A., Wyatt, B. A., Goemann, K., & Hutchinson, G. (2014). Petrogenesis of mantle polymict breccias: Insights into mantle processes coeval with kimberlite magmatism. *Journal of Petrology*, *55*(4), 831–858. https://doi.org/10.1093/petrology/egu008

Giuliani, A., Soltys, A., Phillips, D., Kamenetsky, V. S., Maas, R., Goemann, K., et al. (2017). The final stages of kimberlite petrogenesis: Petrography, mineral chemistry, melt inclusions and Sr-C-O isotope geochemistry of the Bultfontein kimberlite (Kimberley, South Africa). *Chemical Geology*, *455*, 342–356. https://doi.org/10.1016/j.chemgeo.2016.10.011

Griffin, W. L., Spetsius, Z. V., Pearson, N. J., & O'Reilly, S. Y. (2002). In situ Re-Os analysis of sulfide inclusions in kimberlitic olivine: New constraints on depletion events in the Siberian lithospheric mantle. *Geochemistry, Geophysics, Geosystems*, *3*, 1069. https://doi.org/10.1029/2001gc000287

Grinenko, V. A., & Mineyev, S. D. (1992). Low-temperature leaching of sulfur from basic rocks. *Geochemistry International*, *29*, 77–91.

Hanger, B. J., Yaxley, G. M., Berry, A. J., & Kamenetsky, V. S. (2015). Relationships between oxygen fugacity and metasomatism in the Kaapvaal subcratonic mantle, represented by garnet peridotite xenoliths in the Wesselton kimberlite, South Africa. *Lithos*, *212–215*, 443–452. https://doi.org/10.1016/j.lithos.2014.09.030

Hanor, J. S. (2000). Barite-celestine geochemistry and environments of formation. *Reviews in Mineralogy and Geochemistry*, *40*(1), 193–275. https://doi.org/10.2138/rmg.2000.40.4

Hanson, E. K., Moore, J. M., Bordy, E. M., Marsh, J. S., Howarth, G., & Robey, J. V. A. (2009). Cretaceous erosion in central South Africa: Evidence from upper-crustal xenoliths in kimberlite diatremes. *South African Journal of Geology*, *112*, 125–140. https://doi.org/10.2113/gssajg.112.2.125

Hawthorne, J. B. (1968). Kimberlite sills. *South African Journal of Geology*, *71*(3), 291–311.

Hawthorne, J. B. (1975). Model of a kimberlite pipe. *Physics and Chemistry of the Earth*, *9*, 1–15. https://doi.org/10.1016/b978-0-08-018017-5.50005-5

Heaman, L. M. (1989). The nature of the subcontinental mantle from Sr-Nd-Pb isotopic studies on kimberlitic perovskite. *Earth and Planetary Science Letters*, *92*, 323–334. https://doi.org/10.1016/0012-821x(89)90057-5

Heaman, L. M., Phillips, D., & Pearson, D. G. (2019). Dating kimberlites: Methods and emplacement patterns through time. *Elements: An International Magazine of Mineralogy, Geochemistry, and Petrology*, *15*(6), 399–404. https://doi.org/10.2138/gselements.15.6.399

Helz, G. R., & Wyllie, P. J. (1979). Liquidus relationships in the system $CaCO_3$-$Ca(OH)_2$-CaS and the solubility of sulfur in carbonatite magmas. *Geochimica et Cosmochimica Acta*, *43*, 259–265. https://doi.org/10.1016/0016-7037(79)90244-8

Hoare, B. C., Tomlinson, E. L., Barnes, J. D., Tappe, S., Marks, M. A. W., Epp, T., et al. (2021). Tracking halogen recycling and volatile loss in kimberlite magmatism from Greenland: Evidence from combined F-Cl-Br and δ^{37}Cl systematics. *Lithos*, *384–385*, 105976. https://doi.org/10.1016/j.lithos.2021.105976

Holwell, D. A., Fiorentini, M., McDonald, I., Lu, Y., Giuliani, A., Smith, D. J., et al. (2019). A metasomatized lithospheric mantle control on the metallogenic signature of post-subduction magmatism. *Nature Communications*, *10*, 3511. https://doi.org/10.1038/s41467-019-11065-4

Howarth, G. H., & Taylor, L. A. (2016). Multi-step kimberlite evolution tracked in zoned olivine from the Benfontein sill, South Africa. *Lithos*, *262*, 384–397. https://doi.org/10.1016/j.lithos.2016.07.028

Hunter, R. H., & Taylor, L. A. (1982). Instability of garnet from the mantle: Glass as evidence of metasomatic melting. *Geology*, *10*(12), 617–620. https://doi.org/10.1130/0091-7613(1982)10<617:iogftm>2.0.co;2

Hutchison, W., Babiel, R. J., Finch, A. A., Marks, M. A. W., Markl, G., Boyce, A. J., et al. (2019). Sulphur isotopes of alkaline magmas unlock long-term records of crustal recycling on Earth. *Nature Communications*, *10*(1), 1–12. https://doi.org/10.1038/s41467-019-12218-1

Jacob, D. E., Viljoen, K. S., & Grassineau, N. V. (2009). Eclogite xenoliths from Kimberley, South Africa: A case study of mantle metasomatism in eclogites. *Lithos*, *112S*, 1002–1013. https://doi.org/10.1016/j.lithos.2009.03.034

Jelsma, H., Barnett, W., Richards, S., & Lister, G. (2009). Tectonic setting of kimberlites. *Lithos*, *112*, 155–165. https://doi.org/10.1016/j.lithos.2009.06.030

Johnston, D. T., Farquhar, J., Wing, B. A., Kaufman, A. J., Canfield, D. E., & Habicht, K. S. (2005). Multiple sulfur isotope fractionations in biological systems: A case study with sulfate reducers and sulfur disproportionators. *American Journal of Science*, *305*(6–8), 645–660. https://doi.org/10.2475/ajs.305.6-8.645

Kamber, B. S., Greig, A., Schoenberg, R., & Collerson, K. D. (2003). A refined solution to Earth's hidden niobium: Implications for evolution of continental crust and mode of core formation. *Precambrian Research*, *126*, 289–308. https://doi.org/10.1016/s0301-9268(03)00100-1

Kamenetsky, M. B., Sobolev, A. V., Kamenetsky, V. S., Maas, R., Danyushevsky, L. V., Thomas, R., et al. (2004). Kimberlite melts rich in alkali chlorides and carbonates: A potent metasomatic agent in the mantle. *Geology*, *32*(10), 845–848. https://doi.org/10.1130/g20821.1

Kitayama, Y., Thomassot, E., Galy, A., Golovin, A., Korsakov, A., d'Eyrames, E., et al. (2017). Co-magmatic sulfides and sulfates in the Udachnaya-East pipe (Siberia): A record of the redox state and isotopic composition of sulfur in kimberlites and their mantle sources. *Chemical Geology*, *455*, 315–330. https://doi.org/10.1016/j.chemgeo.2016.10.037

Kjarsgaard, B. A., Pearson, D. G., Tappe, S., Nowell, G. M., & Dowall, D. P. (2009). Geochemistry of hypabyssal kimberlites from Lac de Gras, Canada: Comparisons to a global database and applications to the parent magma problem. *Lithos*, *112S*, 236–248. https://doi.org/10.1016/j.lithos.2009.06.001

Kopylova, M. G., Gaudet, M., Kostrovitsky, S. I., Polozov, A. G., & Yakovlev, D. A. (2016). Origin of salts and alkali carbonates in the Udachnaya East kimberlite: Insights from petrography of kimberlite phases and their carbonate and evaporite xenoliths. *Journal of Volcanology and Geothermal Research*, *327*, 116–134. https://doi.org/10.1016/j.jvolgeores.2016.07.003

Kramers, J. D. (1977). Lead and strontium isotopes in Cretaceous kimberlites and mantle-derived xenoliths from Southern Africa. *Earth and Planetary Science Letters*, *34*, 419–431. https://doi.org/10.1016/0012-821x(77)90053-x

Kramers, J. D., Roddick, J. C. M., & Dawson, J. B. (1983). Trace element and isotope studies on veined, metasomatic and "MARID" xenoliths from Bultfontein, South Africa. *Earth and Planetary Science Letters*, *65*, 90–106. https://doi.org/10.1016/0012-821x(83)90192-9

Labidi, J., Cartigny, P., & Moreira, M. (2013). Non-chondritic sulfur isotope composition of the terrestrial mantle. *Nature*, *501*, 208–211. https://doi.org/10.1038/nature12490

Labidi, J., Farquhar, J., Alexander, C. M. O. D., Eldridge, D. L., & Oduro, H. (2017). Mass independent sulfur isotope signatures in CMs: Implications for sulfur chemistry in the early solar system. *Geochimica et Cosmochimica Acta*, *196*, 326–350. https://doi.org/10.1016/j.gca.2016.09.036

Lawless, P. J., Gurney, J. J., & Dawson, J. D. (1979). Polymict peridotites from the Bultfontein and De Beers mines, Kimberley, South Africa. In F. R. Boyd, & H. O. A. Meyer (Eds.), *The mantle sample, 2nd international kimberlite conference* (pp. 145–155). American Geophysical Union. https://doi.org/10.1029/sp016p0145

le Roex, A. P., Bell, D. R., & Davis, P. (2003). Petrogenesis of group I kimberlites from Kimberley, South Africa: Evidence from bulk-rock geochemistry. *Journal of Petrology*, *44*(12), 2261–2286. https://doi.org/10.1093/petrology/egg077

Lorand, J.-P., & Grégoire, M. (2006). Petrogenesis of base metal sulphide assemblages of some peridotites from the Kaapvaal craton (South Africa). *Contributions to Mineralogy and Petrology*, *151*, 521–538. https://doi.org/10.1007/s00410-006-0074-7

Maier, W. D., O'Brien, H., Peltonen, P., & Barnes, S.-J. (2017). Platinum-group element contents of Karelian kimberlites: Implications for the PGE budget of the sub-continental lithospheric mantle. *Geochimica et Cosmochimica Acta*, *216*, 358–371. https://doi.org/10.1016/j.gca.2017.07.002

Marini, L., Moretti, R., & Accornero, M. (2011). Sulfur isotopes in magmatic-hydrothermal systems, melts and magmas. *Reviews in Mineralogy and Geochemistry*, *73*, 423–492. https://doi.org/10.2138/rmg.2011.73.14

Maruoka, T., Koeberl, C., Hancox, P. J., & Reimold, W. U. (2003). Sulfur geochemistry across a terrestrial Permian-Triassic boundary section in the Karoo basin, South Africa. *Earth and Planetary Science Letters*, *206*, 101–117. https://doi.org/10.1016/s0012-821x(02)01087-7

Mitchell, R. H. (1995). *Kimberlites, orangeites, and related rocks*. Springer Science + Business Media, LLC.

Mitchell, R. H. (1986). *Kimberlites: Mineralogy, geochemistry, and petrology*. Springer Science + Business Media.

Mitchell, R. H. (2008). Petrology of hypabyssal kimberlites: Relevance to primary magma compositions. *Journal of Volcanology and Geothermal Research*, *174*(1–3), 1–8. https://doi.org/10.1016/j.jvolgeores.2007.12.024
Mitchell, R. H. (2013). Paragenesis and oxygen isotopic studies of serpentine in kimberlite. In *Proceedings of 10th international Kimberlite conference* (pp. 1–12). Springer. https://doi.org/10.1007/978-81-322-1170-9_1
Mitchell, R. H. (2020). Igneous rock associations 26. Lamproites, exotic potassic alkaline rocks: A review of their nomenclature, characterization and origins. *Geoscience Canada*, *47*, 119–142. https://doi.org/10.12789/geocanj.2020.47.162
Mitchell, R. H., Giuliani, A., & O'Brien, H. (2019). What is a kimberlite? petrology and mineralogy of hypabyssal kimberlites. *Elements*, *15*, 381–386. https://doi.org/10.2138/gselements.15.6.381
Miyoshi, T., Sakai, H., & Chiba, H. (1984). Experimental study of sulfur isotope fractionation factors between sulfate and sulfide in high temperature melts. *Geochemical Journal*, *18*, 75–84. https://doi.org/10.2343/geochemj.18.75
Muramatsu, Y. (1983). Geochemical investigations of kimberlites from the Kimberley area, South Africa. *Geochemical Journal*, *17*, 71–86. https://doi.org/10.2343/geochemj.17.71
Nakanishi, N., Giuliani, A., Carlson, R. W., Horan, M. F., Woodhead, J., Pearson, D. G., & Walker, R. J. (2021). Tungsten-182 evidence for an ancient kimberlite source. *Proceedings of the National Academy of Sciences*, *118*(23). https://doi.org/10.1073/pnas.2020680118
Nowell, G. M., Pearson, D. G., Bell, D. R., Carlson, R. W., Smith, C. B., Kempton, P. D., & Noble, S. R. (2004). Hf isotope systematics of kimberlites and their megacrysts: New constraints on their source regions. *Journal of Petrology*, *45*(8), 1583–1612. https://doi.org/10.1093/petrology/egh024
Ohmoto, H., & Rye, R. O. (1979). Isotopes of sulfur and carbon. In H. L. Barnes (Ed.), *Geochemistry of hydrothermal ore deposits* (2nd ed., pp. 509–567). Wiley.
Pasteris, J. D. (1980). Opaque oxide phases of the De Beers Pipe kimberlite (Kimberley, South Africa) and their petrologic significance. PhD dissertation. Yale University.
Paton, C., Woodhead, J. D., Hergt, J. M., Phillips, D., & Shee, S. (2007). Strontium isotope analysis of kimberlitic groundmass perovskite via LA-MC-ICP-MS. *Geostandards and Geoanalytical Research*, *31*(4), 321–330. https://doi.org/10.1111/j.1751-908x.2007.00131.x
Pearson, D. G., Woodhead, J., & Janney, P. E. (2019). Kimberlites as geochemical probes of Earth's mantle. *Elements*, *15*, 387–392. https://doi.org/10.2138/gselements.15.6.387
Phillips, D., Harris, J. W., & Viljoen, K. S. (2004). Mineral chemistry and thermobarometry of inclusions from De Beers Pool diamonds, Kimberley, South Africa. *Lithos*, *77*, 155–179. https://doi.org/10.1016/j.lithos.2004.04.005
Rudnick, R. L., Eldridge, C. S., & Bulanova, G. P. (1993). Diamond growth history from in situ measurement of Pb and S isotopic compositions of sulfide inclusions. *Geology*, *21*, 13–16. https://doi.org/10.1130/0091-7613(1993)021<0013:dghfis>2.3.co;2
Russell, J. K., Porritt, L. A., Lavallee, Y., & Dingwell, D. B. (2012). Kimberlite ascent by assimilation-fuelled buoyancy. *Nature*, *481*, 352–356. https://doi.org/10.1038/nature10740
Rye, R. O. (2005). A review of the stable-isotope geochemistry of sulfate minerals in selected igneous environments and related hydrothermal systems. *Chemical Geology*, *215*, 5–36. https://doi.org/10.1016/j.chemgeo.2004.06.034
Scaillet, B., & MacDonald, R. (2006). Experimental and thermodynamic constraints on the sulfur yield of peralkaline and metaluminous silicic flood eruptions. *Journal of Petrology*, *47*, 1413–1437. https://doi.org/10.1093/petrology/egl016
Sharygin, V. V., Golovin, A. V., Pokhilenko, N. P., & Kamenetsky, V. S. (2007). Djerfisherite in the Udachnaya-East pipe kimberlites (Sakha-Yakutia, Russia): Paragenesis, composition and origin. *European Journal of Mineralogy*, *19*(1), 51–63. https://doi.org/10.1127/0935-1221/2007/0019-0051
Shee, S. R. (1985). The petrogenesis of the Wesselton mine kimberlite, Kimberley, Cape Province, Republic of South Africa. PhD thesis. University of Cape Town.
Shee, S. R., Clement, C. R., & Skinner, E. M. W. (1994). The petrology of the Wesselton kimberlite sills, Kimberley, Cape Province, South Africa. In H. O. A. Meyer, & O. H. Leonardos (Eds.), *Kimberlites, related rocks and mantle xenoliths. 5th International Kimberlite Conference* (pp. 98–114). CRPM Special Publication.
Skinner, E. M. W., & Clement, C. R. (1979). Mineralogical classification of southern African kimberlites. In *Proceedings of the Second international kimberlite conference* (pp. 129–139). American Geophysical Union. https://doi.org/10.1029/sp015p0129
Smith, C. B. (1983). Pb, Sr and Nd isotopic evidence for sources of southern African Cretaceous kimberlites. *Nature*, *304*, 51–54. https://doi.org/10.1038/304051a0
Smith, R. M. H., Eriksson, P. G., & Botha, W. J. (1993). A review of the stratigraphy and sedimentary environments of the Karoo-aged basins of Southern Africa. *Journal of African Earth Sciences*, *16*, 143–169. https://doi.org/10.1016/0899-5362(93)90164-l
Soltys, A., Giuliani, A., & Phillips, D. (2018a). Crystallisation sequence and magma evolution of the De Beers dyke (Kimberley, South Africa). *Mineralogy and Petrology*, *112*, 503–518. https://doi.org/10.1007/s00710-018-0588-5
Soltys, A., Giuliani, A., & Phillips, D. (2018b). A new approach to reconstructing the composition and evolution of kimberlite melts: A case study of the archetypal Bultfontein kimberlite (Kimberley, South Africa). *Lithos*, *304–307*, 1–15. https://doi.org/10.1016/j.lithos.2018.01.027
Soltys, A., Giuliani, A., & Phillips, D. (2020). Apatite compositions and groundmass mineralogy record divergent melt/fluid evolution trajectories in coherent kimberlites caused by differing emplacement mechanisms. *Contributions to Mineralogy and Petrology*, *175*(5). https://doi.org/10.1007/s00410-020-01686-0
Soltys, A., Giuliani, A., Phillips, D., & Kamenetsky, V. S. (2020). Kimberlite metasomatism of the lithosphere and the evolution of olivine in carbonate-rich melts—Evidence from the Kimberley kimberlites (South Africa). *Journal of Petrology*. https://doi.org/10.1093/petrology/egaa062/5857610
Sparks, R. S. J. (2013). Kimberlite volcanism. *Annual Review of Earth and Planetary Sciences*, *41*, 497–528. https://doi.org/10.1146/annurev-earth-042711-105252
Stamm, N., & Schmidt, M. W. (2017). Asthenospheric kimberlites: Volatile contents and bulk compositions at 7 GPa. *Earth and Planetary Science Letters*, *474*, 309–321. https://doi.org/10.1016/j.epsl.2017.06.037
Stripp, G. R., Field, M., Schumacher, C., Sparks, R. S. J., & Cressey, G. (2006). Post-emplacement serpentinization and related hydrothermal metamorphism in a kimberlite from Venetia, South Africa. *Journal of Metamorphic Geology*, *24*, 515–534. https://doi.org/10.1111/j.1525-1314.2006.00652.x
Sun, Z., Xiong, X., Wang, J., Liu, X., Li, L., Ruan, M., et al. (2020). Sulfur abundance and heterogeneity in the MORB mantle estimated by copper partitioning and sulfur solubility modelling. *Earth and Planetary Science Letters*, *538*, 116169. https://doi.org/10.1016/j.epsl.2020.116169
Tappe, S., Brand, N. B., Stracke, A., van Acken, D., Liu, C. Z., Strauss, H., et al. (2017). Plates or plumes in the origin of kimberlites: U/Pb perovskite and Sr-Nd-Hf-Os-C-O isotope constraints from the Superior craton (Canada). *Chemical Geology*, *455*, 57–83. https://doi.org/10.1016/j.chemgeo.2016.08.019

Tappe, S., Budde, G., Stracke, A., Wilson, A., & Kleine, T. (2020). The tungsten-182 record of kimberlites above the African superplume: Exploring links to the core-mantle boundary. *Earth and Planetary Science Letters*, *547*, 116473. https://doi.org/10.1016/j.epsl.2020.116473

Tappe, S., Pearson, D. G., Kjarsgaard, B. A., Nowell, G., & Dowall, D. (2013). Mantle transition zone input to kimberlite magmatism near a subduction zone: Origin of anomalous Nd-Hf isotope systematics at Lac de Gras, Canada. *Earth and Planetary Science Letters*, *371–372*, 235–251. https://doi.org/10.1016/j.epsl.2013.03.039

Tappe, S., Romer, R. L., Stracke, A., Steenfelt, A., Smart, K. A., Muehlenbachs, K., & Torsvik, T. H. (2017). Sources and mobility of carbonate melts beneath cratons, with implications for deep carbon cycling, metasomatism and rift initiation. *Earth and Planetary Science Letters*, *466*, 152–167. https://doi.org/10.1016/j.epsl.2017.03.011

Tappe, S., Smart, K., Torsvik, T., Massuyeau, M., & de Wit, M. (2018). Geodynamics of kimberlites on a cooling Earth: Clues to plate tectonic evolution and deep volatile cycles. *Earth and Planetary Science Letters*, *484*, 1–14. https://doi.org/10.1016/j.epsl.2017.12.013

Tappe, S., Stracke, A., van Acken, D., Strauss, H., & Luguet, A. (2020). Origins of kimberlites and carbonatites during continental collision—Insights beyond decoupled Nd-Hf isotopes. *Earth-Science Reviews*, *208*, 103287. https://doi.org/10.1016/j.earscirev.2020.103287

Taylor, H. P., Jr., & Sheppard, S. M. F. (1986). Igneous rocks: I. Processes of isotopic fractionation and isotope systematics. *Reviews in Mineralogy and Geochemistry*, *16*(1), 227–272. https://doi.org/10.1515/9781501508936-013

Thode, H., Monster, J., & Dunford, H. (1961). Sulfur isotope geochemistry. *Geochimica et Cosmochimica Acta*, *25*, 159–174. https://doi.org/10.1016/0016-7037(61)90074-6

Thomassot, E., Cartigny, P., Harris, J. W., Lorand, J. P., Rollion-Bard, C., & Chaussidon, M. (2009). Metasomatic diamond growth: A multi-isotope study (13C, 15N, 33S, 34S) of sulphide inclusions and their host diamonds from Jwaneng (Botswana). *Earth and Planetary Science Letters*, *282*, 79–90. https://doi.org/10.1016/j.epsl.2009.03.001

Tovey, M., Giuliani, A., Phillips, D., Pearson, D. G., Sarkar, C., Nowicki, T., & Carlson, J. (2021). The spatial and temporal evolution of primitive melt compositions within the Lac de Gras kimberlite field, Canada: Source evolution vs lithospheric mantle assimilation. *Lithos*, *392–393*, 106142. https://doi.org/10.1016/j.lithos.2021.106142

Tsai, H., Shieh, Y., & Meyer, H. O. A. (1979). Mineralogy and $^{34}S/^{32}S$ ratios of sulfides associated with kimberlite, xenoliths, and diamonds. In F. R. Boyd, & H. O. A. Meyer (Eds.), *The mantle sample, 2nd international kimberlite conference* (pp. 87–103). American Geophysical Union. https://doi.org/10.1029/sp016p0087

Vinogradov, V., & Ilupin, I. (1972). Isotope compositions of sulfur in kimberlites of the Siberian Platform. *Doklady Akademii Nauk USSR*, 221–223.

Wagner, P. A. (1914). *The diamond fields of South Africa*. pp 347. Transvaal Leader.

White, J. L., Sparks, R. S. J., Bailey, K., Barnett, W. P., Field, M., & Windsor, L. (2012). Kimberlite sills and dykes associated with the Wesselton kimberlite pipe, Kimberley, South Africa. *South African Journal of Geology*, *115*, 1–32. https://doi.org/10.2113/gssajg.115.1.1

Whitelaw, H. T., de Bruiyn, H., Schoch, A. E., van der Westhuizen, W. A., & Kruger, F. J. (2005). Isotopic relationships of epigenetic Pb-Zn mineralisation in the Ventersdorp Supergroup near Douglas, Northern Cape Province. *South African Journal of Geology*, *108*, 187–198. https://doi.org/10.2113/108.2.187

Williams, A. F. (1932). *The genesis of diamonds*. Ernest Benn Ltd.

Wilson, M. R., Kjarsgaard, B. A., & Taylor, B. (2007). Stable isotope composition of magmatic and deuteric carbonate phases in hypabyssal kimberlite, Lac de Gras field, Northwest Territories, Canada. *Chemical Geology*, *242*, 435–454. https://doi.org/10.1016/j.chemgeo.2007.05.002

Woodhead, J., Hergt, J., Giuliani, A., Maas, R., Phillips, D., Pearson, D. G., & Nowell, G. (2019). Kimberlites reveal 2.5-billion-year evolution of a deep, isolated mantle reservoir. *Nature*, *573*, 578–581. https://doi.org/10.1038/s41586-019-1574-8

Woodhead, J., Hergt, J., Phillips, D., & Paton, C. (2009). African kimberlites revisited: In situ Sr-isotope analysis of groundmass perovskite. *Lithos*, *112*, 311–317. https://doi.org/10.1016/j.lithos.2009.03.031

Woodland, A. B., Girnis, A. V., Bulatov, V. K., Brey, G. P., & Höfer, H. E. (2019). Experimental study of sulfur solubility in silicate-carbonate melts at 5–10.5 GPa. *Chemical Geology*, *505*, 12–22. https://doi.org/10.1016/j.chemgeo.2018.12.008

Zhang, H.-F., Mattey, D. P., Grassineau, N., Lowry, D., Brownless, M., Gurney, J. J., & Menzies, M. A. (2000). Recent fluid processes in the Kaapvaal Craton, South Africa: Coupled oxygen isotope and trace element disequilibrium in polymict peridotites. *Earth and Planetary Science Letters*, *176*, 57–72. https://doi.org/10.1016/s0012-821x(99)00311-8

Zhu, R. Z., Ni, P., Wang, G. G., Ding, J. Y., & Kang, N. (2021). Temperature and oxygen state of kimberlite magma from the North China Craton and their implication for diamond survival. *Mineralium Deposita*, 1–18. https://doi.org/10.1007/s00126-021-01057-0